Multi-element polynomial chaos expansion based on automatic discontinuity detection for nonlinear systems

Juliette Dréau, Benoit Magnain, Alain Batailly

POLYTECHNIQUE MONTRÉAL
UNIVERSITÉ D'INGÉNIERIE

LABORATOIRE D'ANALYSE VIBRATOIRE ET ACOUSTIQUE

Multi-element polynomial chaos expansion based on automatic discontinuity detection for nonlinear systems

Juliette Dréau[1], Benoit Magnain[2], Alain Batailly[1]

Abstract

This article focuses on the stochastic modeling of nonlinear systems featuring discontinuities in their response surface. More specifically, original developments are presented to improve the efficiency of multi-element polynomial chaos expansion for such systems. First, an automated detection procedure of the discontinuities is proposed. It relies on an iterative algorithm with a polynomial annihilation edge detection method and support vector machine classification algorithms leading to the representation of the discontinuity as a B-spline curve. Based on this curve, an *ad-hoc* decomposition of the variable space is considered and an original approach for the application of polynomial chaos expansion on each subdomain yields a robust and versatile way to compute the response surface of the system of interest. The proposed methodology is detailed and applied to several nonlinear academic systems such as a circular discontinuity and the Duffing oscillator including one or two discontinuities in its response surface. Through these applications, it is evidenced that, compared to the classical polynomial chaos and multi-element polynomial chaos expansions, the proposed methodology yields an approximation of the discontinuous responses that is both more accurate and less computationally expensive. The influence of the main parameters of the proposed methodology is also analyzed in details. This parametric analysis underlines the robustness of the methodology and highlights the key parameters in terms of computational cost and accuracy of the discontinuities. The proposed methodology is finally applied to an industrial application, it allows to efficiently compute the surface response of an industrial compressor blade undergoing structural contacts.

Keywords

Polynomial Chaos Expansion, Multi-element, Discontinuity Detection, Polynomial Annihilation, Support Vector Machines, Uncertainty quantification.

1 - Department of Mechanical Engineering, École Polytechnique de Montréal, P.O. Box 6079, Succ. Centre-Ville, Montréal, Québec, Canada H3C 3A7
2 - LaMé, EA 7494, INSA CVL, Univ. Orléans, Univ. Tours, F-18020, Bourges Cedex, France

Chaos polynomial multi-élément et détection automatique de discontinuités pour les systèmes non linéaires

Juliette Dréau[1], Benoit Magnain[2], Alain Batailly[1]

Résumé

Cet article porte sur la modélisation stochastique de systèmes non linéaires présentant une discontinuité dans leur surface de réponse. Plus précisément, des développements originaux sont présentés pour appliquer la méthode du chaos polynomial multi-élément à de tels systèmes. Une procédure de détection automatique des discontinuités est tout d'abord présentée. Elle repose sur un algorithme itératif avec détection de bords par annihilation polynomiale et sur une classification par machines à vecteurs de support permettant de représenter la discontinuité par une courbe paramétrique de type B-spline. Sur base de cette courbe, une décomposition *ad hoc* de l'espace des variables est effectuée pour permettre une application de la méthode du chaos polynomial sur chacun des sous-domaines. La méthodologie proposées est détaillée et appliquée à plusieurs systèmes académiques incluant une discontinuité de forme circulaire et un oscillateur de Duffing. Ces applications permettent de mettre en évidence que, contrairement à la méthode classique du chaos multi-élément, la méthodologie proposée aboutit à une approximation de la surface de réponse qui est à la fois précise et peu coûteuse numériquement. L'influence de chacun des principaux paramètres de la méthode est analysée en détails pour souligner la robustesse de l'approche proposée. Enfin, une application industrielle est proposée pour démontrer le potentiel de la méthodologie proposée pour obtenir la surface de réponse d'une aube de compresseur soumise à des contacts structuraux.

Mots-clés

Chaos polynomial, multi-élément, détection de discontinuité, annihilation polynomiales, machines à vecteurs de support, quantification d'incertitude.

1 - Département de génie mécanique, École Polytechnique de Montréal, P.O. Box 6079, Succ. Centre-Ville, Montréal, Québec, Canada H3C 3A7
2 - LaMé, EA 7494, INSA CVL, Univ. Orléans, Univ. Tours, F-18020, Bourges Cedex, France

1 Introduction

To a certain degree, all complex engineering systems are intrinsically nonlinear. In practice, the influence of this nonlinearity over a system's nominal operating range may not always be significant. However, specific design issues arise when it becomes impossible to neglect the nonlinear behavior of a mechanical system, be it due to contact or friction interfaces for instance. In this situation, designers are facing a theoretical roadblock as there exists no unified theoretical framework for the analysis of nonlinear mechanical systems. As a consequence, there has been a vast amount of research works dedicated to the development of *ad-hoc* predictive numerical strategies with the intent to (1) better understand the underlying physical phenomena and (2) provide designers with the tools they need for the *a posteriori* discrimination of better suited design solutions.

As the developed predictive numerical strategies become more robust, accurate and computationally efficient, there is a drive towards their inclusion in early design stages. Should designers be able to identify key design parameters or guidelines to mitigate nonlinear interactions, this could lead to the design of safer and more robust mechanical systems. In the meantime, predictive numerical strategies can be used to provide essential design data such as the system's response surface over selected parameters' ranges of variation. Be it for uncertainty quantification [1, 2] or the identification of an ideal operating point, response surfaces are key in many engineering applications. Unfortunately, for large mechanical systems featuring several nonlinear interfaces or combining distinct types of nonlinearities, the computational effort required for these response surfaces may not be acceptable in an industrial context.

Alternative ways to compute these response surfaces must thus be found. Spectral methods [3, 4], including the well-known polynomial chaos expansion (PCE) [5], have therefore emerged in recent decades. In particular, PCE has been widely applied in an industrial context [6, 7, 8, 9] and extended to a wide variety of probability distributions under the name of generalized PCE (gPCE) [10] based on intrusive [11] or non intrusive [12] approaches. However, in the case of nonlinear mechanical systems, it is likely that their response surfaces feature discontinuities or localized strong variations. Because gPCE relies on smooth polynomial interpolation, it is ill-suited for capturing such phenomena [13]. In order to mitigate this issue, a multi-element gPCE (ME-gPCE) has been developed [13], it relies on a decomposition of the random space into several elements over which gPCE may be applied. This method has been referred to as a piecewise gPCE [14]. ME-gPCE typically relies on a decomposition of the random space using a tensor structure with rectangular shape [15, 16, 17]. However, using such decomposition, a very large number of elements may be required to accurately capture discontinuities of the response surface.

Because it is of paramount importance to accurately locate such discontinuities on a response surface, the detection of discontinuities itself has generated a large number of research works over the last years. In particular, edge detection techniques [18, 19] have been developed to accurately represent discontinuities over a 2D response surface. Discontinuities are commonly detected by means of the polynomial annihilation edge detection method [18] and the discontinuity itself may be represented using support vector machine (SVM) [19]. Other methods based on Bayesian inference techniques can be used to locate a discontinuity [20]. Recently, ME-gPCE itself has been used to detect discontinuities [21]. Once the discontinuity has been detected, an approximation method such as gPCE is performed to interpolate the system response on each subdomain [22, 23, 24]. These methods are mostly multi-element probabilistic collocation methods [25] based on least orthogonal interpolation [26]. With respect to ME-gPCE, its application relies on a regression method [12] and it has not yet been coupled with a detection of discontinuities method.

In this paper, a new method combining multi-element generalized polynomial chaos expansion and discontinuity detection is proposed to decompose the random space into a minimal number of subdomains over which gPCE is then applied. An automatic discontinuity detection is proposed based on polynomial annihilation edge detection method [18]. Discontinuity localization also relies on support vector machine classification algorithms to accurately represent the discontinuities. The discontinuities detected are then used as element boundaries in the ME-gPCE to propose a random space decomposition adapted to the discontinuities of the system. The ME-gPCE is therefore used on subdomains related to the discontinuity of the model response.

This paper is divided into five sections, excluding the introduction and the conclusion. Section 2 of this article is dedicated to the presentation of gPCE and ME-gPCE when applied to discontinuous response surfaces, and their limitations are highlighted on academic nonlinear systems. The objective and the steps of the proposed

two-phase methodology are also presented. The first phase of the proposed methodology is the automated detection of discontinuities, proposed developments are detailed in the section 3. In section 4, the second phase related to the response surface approximation is presented. The proposed methodology is applied on academic nonlinear systems such as a benchmark function used in the literature [22] and the Duffing oscillator. In section 5, the influence of key parameters of the proposed methodology is analyzed on an academic nonlinear system. Finally, in the last section of the article, the proposed methodology is applied to obtain the response surface of a compressor blade undergoing structural contacts considering two variables: the angular speed of the blade and the blade-tip/casing clearance.

2 Context

The use of spectral methods such as generalized polynomial chaos expansion is facing a roadblock when considering mechanical systems featuring a discontinuous response surface. For such systems, the fact that gPCE relies on polynomial interpolation yields spurious oscillations of the approximated response surface which significantly alters its accuracy. In this section, this phenomenon is first briefly illustrated with the well-known Duffing oscillator before an overview of the proposed methodology to tackle this issue be presented. The Duffing oscillator is used throughout the methodology sections of the article for illustrative purposes.

2.1 Example of a discontinuous response surface: the Duffing oscillator

The Duffing oscillator is a one-degree-of-freedom nonlinear oscillator characterized by the following equation of motion:

$$m\ddot{u} + c\dot{u} + ku + k_{\mathrm{nl}}u^3 = F\cos(\omega t), \tag{1}$$

where m, c, k and k_{nl} are respectively the mass, damping coefficient, linear stiffness and nonlinear stiffness. $F\cos(\omega t)$ is the excitation force of pulsation ω, and u, $\dot{u}$ and $\ddot{u}$ stand for the displacement and its first and second derivatives with respect to time. The values of the parameters considered in this study are detailed in Tab. 1.

variable	description	value	unit
m	mass	1	kg
c	damping coefficient	0.25	$\mathrm{N\cdot s\cdot m^{-1}}$
k	linear stiffness	$[0, 0.5]$	$\mathrm{N\cdot m^{-1}}$
k_{nl}	nonlinear stiffness	0.5	$\mathrm{N/m^3}$
F	excitation force amplitude	$[0, 1]$	N
ω	pulsation	1	$\mathrm{rad\cdot s^{-1}}$

Table 1. Mechanical parameters of the Duffing oscillator.

The linear stiffness k and the amplitude F of the excitation force are here considered as random variables, uniformly distributed on $\Omega = [0, 0.5] \times [0, 1]$. Assuming null initial conditions, Eq. (1) is solved for 10,000 couples of values (k, F) using an ordinary differential equation solver based on lsoda from the FORTRAN ODE library [27, 28]. The 10,000 samples are computed based on a regular 100×100 grid over Ω and the corresponding response surface—representing $\mathcal{D}(k, F) = \max(u(t))$ over the last two of the twenty simulated periods T with $t \in [0, 40\pi]$, and which will be used here as a reference point—is shown in Fig. 1. As evidenced in Fig. 1, the response surface of the Duffing oscillator over Ω is discontinuous.

2.2 Approximation of a discontinuous response surface

An approximation of the response surface depicted in Fig. 1 is first obtained using gPCE [10]. gPCE coefficients are computed based on a 81-equidistant point design of experiments (a regular grid of 9×9 equidistant point over Ω, see (○) in Fig. 2(a)) and a high value of the degree of interpolation ($q = 7$). Assuming a uniform distribution

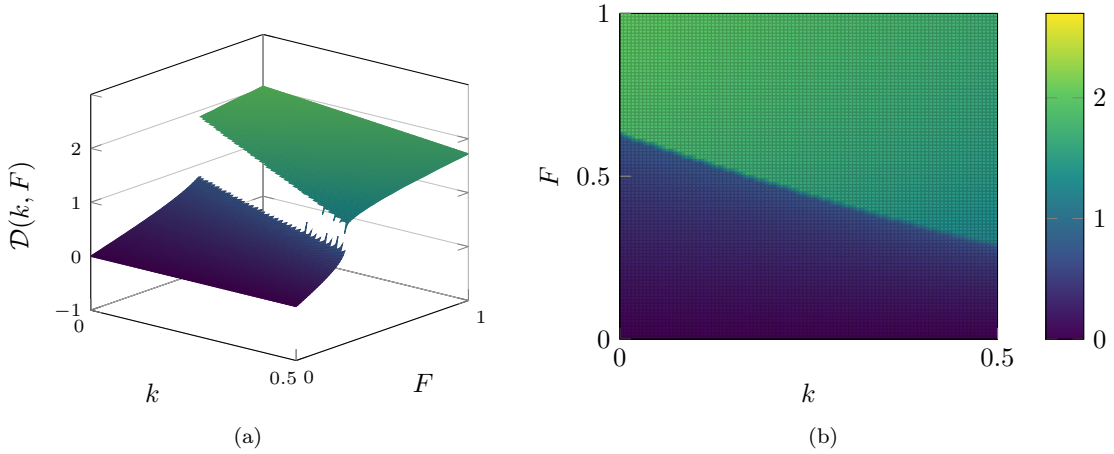

Figure 1. Duffing oscillator, reference response surface over Ω: (a) 3D view; (b) 2D view.

of variables, gPCE basis is composed of Legendre polynomials. The corresponding approximated response surface is then plotted using the 10,000 couples of values (k, F) previously drawn for the reference response surface, see Fig. 2(a). An overview of the distribution of the error with respect to the reference response surface, denoted E, is plotted in Fig. 2(b). Due to its very definition, gPCE cannot capture the discontinuity of the response surface

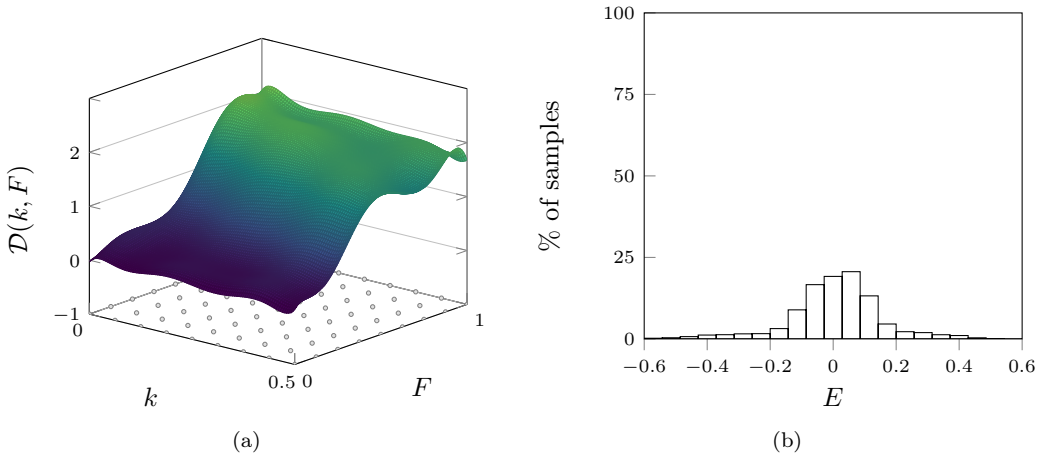

Figure 2. Approximation of Duffing oscillator response surface by gPCE: (a) approximated response surface from points (◎) in the design of experiments; (b) error distributions with respect to the reference response surface.

thus yielding significant errors in the approximation of the response surface. Because of spurious oscillations that propagate throughout the response surface, non negligible errors are found throughout Ω.

Multi-Element generalized polynomial chaos expansion [13] is one of the strategies developed in order to overcome the limitations of gPCE. It is here applied with a decomposition of the random space Ω within 16 rectangular subdomains. Over each of these subdomains, gPCE is applied with $q = 2$ using a 9-point uniform design of experiments. The *a priori* decomposition of the random space implies that it cannot account for the location of the response surface discontinuity. The approximated response surface is plotted in Fig. 3(a) using the 10,000 reference samples. Same as for gPCE, the distribution of the error E computed for each sample is shown in Fig. 3(b). For each subdomain where the reference response surface is continuous, ME-gPCE yields excellent results. Where the reference

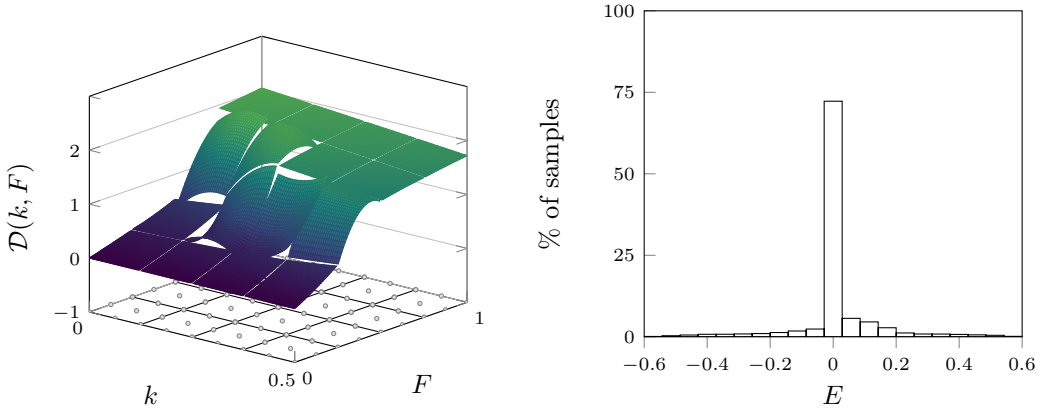

Figure 3. Approximation of Duffing oscillator response surface by ME-gPCE with 16 rectangular elements (—): (a) approximated response surface from points (○) in the design of experiments; (b) error distributions with respect to the reference response surface.

response surface is discontinuous however, ME-gPCE yields significant errors. ME-gPCE thus advantageously yields more localized errors but which remain significant. Based on similar observations, some researchers have proposed to consider a much greater number of subdomains [15] but this may lead to very high number of required evaluations of the response surface that may not be computationally feasible for large nonlinear mechanical systems. Adaptive methods [29] are known to locally increase the number of subdomains in an adaptive manner which often implies a significant computational cost. Contrary to the proposed developments, these methods typically rely on rectangular subdomains. One may also note that ME-gPCE yields a discontinuous response surface.

2.3 Problem statement and overview of the proposed methodology

Let f be a piecewise-continuous function defined over $\Omega \subset \mathbb{R}^2$ by:

$$\begin{aligned} f &: \Omega \to \mathbb{R}, \\ \mathbf{x} &\mapsto f(\mathbf{x}), \end{aligned} \tag{2}$$

A point $\mathbf{x} \in \Omega$ is denoted $\mathbf{x} = [x_1, x_2]$. By definition, f is continuous at a point $\mathbf{x}$ if it verifies:

$$\lim_{\boldsymbol{\Delta} \to \mathbf{0}} f(\mathbf{x} + \boldsymbol{\Delta}) = f(\mathbf{x}) \quad \forall \boldsymbol{\Delta} \in \Omega. \tag{3}$$

Otherwise, it is said to be discontinuous at $\mathbf{x}$. It can be shown that the function $\mathcal{D}$ introduced in the previous subsection is only piecewise-continuous over Ω as it was evidenced that its response surface is discontinuous at certain points. As illustrated above, approximating the response surface of such function is a difficult task. However, it is of high engineering relevance considering most mechanical systems feature a certain degree of nonlinearity which may translate into a discontinuous response surface.

Based on the ME-gPCE, this article introduces an original methodology for the approximation of a piecewise-continuous function with an automated detection procedure of the discontinuities and an *ad-hoc* definition of subdomains in order to minimize the computational cost of the approximation. It relies on two distinct phases that are detailed in the following sections:

1. **automated detection of discontinuities** relying on a two-step approach, which is based on an existing methodology [19]: (1) iterative edge detection, and (2) localized mesh refinement to accurately represent the discontinuities by means of B-spline curves,
2. **approximation of the response surface** using a decomposition of the random space coherent with the detected discontinuities, for an optimal application of ME-gPCE.

Each phase of the proposed methodology is detailed in the following sections. While the automated discontinuity detection method is based on existing methods [18, 19], it has several original features: (1) discontinuities are defined by B-splines [30] used for the decomposition of the domain Ω; (2) point labeling is performed along with iterative edge detection in order to efficiently select new points to be evaluated; (3) repeatability of the discontinuity obtained by support vector machine is ensured by deterministic selection of the training and test sets. Moreover, compared to existing approximation methods [22, 23, 24], ME-gPCE is applied here with coefficient computation by regression method [12], and the decomposition of the random space is carried out by considering subdomains of any shape defined from the previously detected discontinuities.

2.4 Academic systems

The proposed methodology is applied on three academic systems: (1) the previously introduced Duffing oscillator with the response surface plotted in Fig. 1, (2) the Duffing oscillator to which a discontinuity is added to the response surface as shown in Fig. 4(a), and (3) a benchmark function used in the literature [22] as represented in Fig. 4(b). For the second test case, the quantity $D(k, F)$ is the response of the Duffing oscillator introduced in section 2.1 if $(k-0.5)^2 + (F-1)^2 > 0.25^2$, otherwise:

$$\mathcal{D}(k, F) = 3 - k - F + \frac{\exp\left((k+F)^2\right)}{8}. \tag{4}$$

The two phases of the proposed methodology are detailed in the following sections.

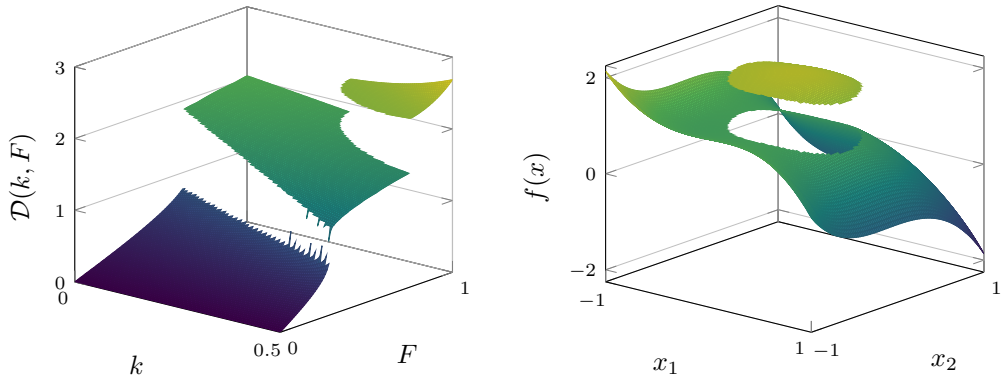

Figure 4. Reference response surfaces of two academic systems: (a) Duffing oscillator with added discontinuity; (b) circular discontinuity [22].

3 Automated detection of discontinuities

3.1 Notations and definitions

In order to assess the possible discontinuity of a function f at a given point $\mathbf{x}$, one may use the jump function δf defined as:

$$\begin{aligned} \delta f &: \Omega \to \mathbb{R}, \\ &\mathbf{x} \mapsto \max_{\boldsymbol{\Delta} \in \Omega} \left(f(\mathbf{x}^+) - f(\mathbf{x}^-) \right), \end{aligned} \tag{5}$$

where $f(\mathbf{x}^+) = \lim_{\epsilon \to 0} f(\mathbf{x} + \epsilon\Delta)$, $f(\mathbf{x}^-) = \lim_{\epsilon \to 0} f(\mathbf{x} - \epsilon\Delta)$ and $\epsilon \in \mathbb{R}$. Should f be discontinuous at $\mathbf{x}$, then $\delta f(\mathbf{x}) \neq 0$.

From a numerical standpoint, the evaluation of both f and δf relies on a discretization of the random space Ω. Based on a set of points $\mathcal{X}^{(k)}$, a Delaunay triangulation $\mathcal{T}^{(k)}$ is computed at each iteration k of the proposed methodology so that:

$$\mathcal{X}^{(k)} = \{\mathbf{x}_1, \dots, \mathbf{x}_{n_k}\},\ k \in \mathbb{N}, \tag{6}$$

and:

$$\mathcal{T}^{(k)} = \{\mathbf{T}_j^{(k)} | \mathbf{T}_j^{(k)} = \{\mathbf{x}_{j_1}, \mathbf{x}_{j_2}, \mathbf{x}_{j_3}\} \subset \left(\mathcal{X}^{(k)}\right)^3\ \forall j \in [\![1, t_k]\!]\}, \tag{7}$$

where $\mathbf{T}_j^{(k)}$ is the set of vertices of triangle element indexed j. The initial mesh $\mathcal{T}^{(0)}$ is built from the set $\mathcal{X}^{(0)}$ which contains n_0 points so that $n_k = n_0 + k$. Based on a n_0-point regular grid of the random space Ω, each point of $\mathcal{X}^{(0)}$ is randomly located in a close vicinity of the regular grid points as shown in Fig. 5. This randomization prevents potential numerical errors should a discontinuity be perfectly aligned with the regular grid. It should be

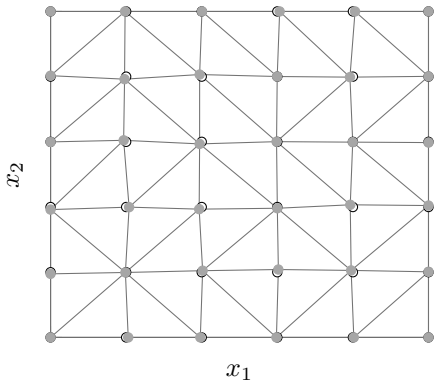

Figure 5. Example of initial mesh $\mathcal{T}^{(0)}$ with 36 points (●) alongside the base regular grid (○).

underlined that, from a numerical standpoint, because f may only be evaluated at a given set of points, the notion of discontinuity is here extended so as to include functions that may locally feature very strong variations. For the sake of simplicity, the term *discontinuous* will be used in the remainder to refer to both actual discontinuous functions and functions that locally feature very strong variations. As a consequence, the term *discontinuity* will be employed to refer to both actual discontinuous areas on the response surface as well as areas with strong variations.

3.2 Step 1: iterative edge detection

In this article, edge detection over Ω relies on a previously published procedure based on polynomial annihilation [18]. Key aspects of this methodology are recalled in the first subsection for the sake of completeness, the reader may refer to the original publication [18] for more details. The following subsections focus on the first contribution of this article: an iterative algorithm developed to get a finer approximation of discontinuities' locations.

3.2.1 Edge detection through polynomial annihilation

The principle behind the employed edge detection procedure is to approximate the jump function δf defined in Eq. (5) using polynomial annihilation [18]. The notation Π_m is used to refer to the space of all polynomials of 2 variables and of degree less or equal to m. The dimension of Π_m is $m_2 = (m+2)!/(m!2!)$. For a given point $\mathbf{y} \in \Omega$, a set $\mathcal{S}^{(k)}$ of m_2 neighboring points is first selected among $\mathcal{X}^{(k)}$:

$$\mathcal{S}^{(k)} = \{\mathbf{x}_{\beta_1}, \dots, \mathbf{x}_{\beta_{m_2}}\},\quad \beta_1, \dots, \beta_{m_2} \in [\![1, n_k]\!]. \tag{8}$$

The following linear system is considered [18]:

$$\sum_{\mathbf{x}_{\beta_i} \in \mathcal{S}^{(k)}} c_i(\mathbf{y}) p_l(\mathbf{x}_{\beta_i}) = \sum_{\|\alpha\|_1 = m} p_{l,\alpha}(\mathbf{y}),\quad \forall l \in [\![1, m_2]\!], \tag{9}$$

where α is a multivariate nonnegative integer, p_l, $l = 1, \ldots, m_2$, is a basis of Π_m and the $p_{l,\alpha}$ refers to the α derivative of p_l. The solution of the linear system (9) yields the values of the coefficients $c_i(\mathbf{y})$, $i = 1, \ldots, m_2$. It is then possible to compute the value of the *edge detector function* [18] $\mathcal{L}_m f(\mathbf{y})$:

$$\mathcal{L}_m f(\mathbf{y}) = \frac{1}{q_m(\mathbf{y})} \sum_{\mathbf{x}_{\beta_i} \in \mathcal{S}^{(k)}} c_i(\mathbf{y}) f(\mathbf{x}_{\beta_i}), \tag{10}$$

where q_m is a normalization factor depending on $\mathcal{S}^{(k)}$ [18]. In practice, the performance of polynomial annihilation is improved by means of the minmod function:

$$\mathcal{L}_{\mathcal{M}} f(\mathbf{y}) = \begin{cases} \min\limits_{m \in \mathcal{M}} \mathcal{L}_m f(\mathbf{y}) & \text{if } \mathcal{L}_m f(\mathbf{y}) > 0 \ \forall m \in \mathcal{M}, \\ \max\limits_{m \in \mathcal{M}} \mathcal{L}_m f(\mathbf{y}) & \text{if } \mathcal{L}_m f(\mathbf{y}) < 0 \ \forall m \in \mathcal{M}, \\ 0 & \text{otherwise,} \end{cases} \tag{11}$$

where the finite set of positive integers $\mathcal{M} \subset \mathbb{N}$ is equal to $\mathcal{M} = \{1, 2, 3, 4\}$ in this study. In the following, it is assumed that $\mathcal{L}_{\mathcal{M}} f(\mathbf{y})$ provides a good approximation of $\delta f(\mathbf{y})$:

$$\delta f(\mathbf{y}) \simeq \mathcal{L}_{\mathcal{M}} f(\mathbf{y}). \tag{12}$$

3.2.2 Iterative algorithm

In order to increase the accuracy of the computation of $\delta f(\mathbf{y})$, it is here proposed to encompass polynomial annihilation edge detection within an iterative algorithm featuring an automated update of the mesh. An overview of the algorithm is given in Fig. 6. This algorithm yields a refinement of the initial mesh specifically in the areas where the jump function takes its highest values and where may lie a discontinuity, it relies on four substeps:

INITIALIZATION the random space is meshed (resulting in $\mathcal{T}^{(0)}$) from an initial set of n_0 points $\mathcal{X}^{(0)}$ where the system's response is computed,

MESH ANALYSIS the edge detector function $\mathcal{L}_{\mathcal{M}} f(\mathbf{y}_j^{(k)})$ is computed at the barycenter $\mathbf{y}_j^{(k)}$ of all elements of the current mesh $\mathcal{T}^{(k)}$. One may note that from an iteration to another, many elements of $\mathcal{T}^{(k)}$ are not changed so that these computations only need to be performed on a limited number of elements,

IDENTIFICATION OF A SUITABLE ELEMENT the element $\mathbf{T}_i^{(k)}$ for which the edge detector function $\mathcal{L}_{\mathcal{M}} f(\mathbf{y}_j^{(k)})$ is maximal is where a point may be added. The new point $\mathbf{x}_{n_0+k+1}$ is selected half way between the two vertices $\mathbf{x}_{i^+}$ and $\mathbf{x}_{i^-}$ of the element which verifies that their evaluation $f(\mathbf{x}_{i^+})$ and $f(\mathbf{x}_{i^-})$ are respectively the highest and the lowest among the three vertices of the element $\mathbf{T}_i^{(k)}$.

REMESHING when a new point $\mathbf{x}_{n_0+k+1}$ has been added, it yields a local remeshing that modifies $\mathcal{T}^{(k)}$.

There are three distinct stopping criteria relating to: (1) a minimal value of the edge detector function $\lambda_L \mathcal{L}_{\mathcal{M}} f_{\max}$, (2) a minimal distance λ_{dist} between two points in $\mathcal{X}^{(k)}$ in order to prevent point clustering, and (3) a maximal number of iterations $k_{\max}$ for which the procedure is stopped. At the end of the procedure, the number of iterations k_{ed} is stored.

3.2.3 Point labeling

Within the algorithm presented in Fig. 6, between the substeps of IDENTIFICATION OF A SUITABLE ELEMENT and REMESHING, a labeling procedure is employed to discriminate each point depending on its position with respect to the discontinuity. This labeling procedure has been implemented within the iterative algorithm but could also be carried out as a post-processing operation since labeling does not affect the definition of $\mathcal{X}^{(k)}$. This is the reason why it is here presented separately. More specifically, two classes of points, $+1$ or -1 are considered based on the evaluation of f. At each iteration k, it is first checked if points $\mathbf{x}_{i-}$ and $\mathbf{x}_{i+}$ belong to $\mathcal{X}^{(0)}$:

$$\begin{cases} \text{label}(\mathbf{x}_{i-}) = -1 & \text{if } \mathbf{x}_{i-} \in \mathcal{X}^{(0)}, \\ \text{label}(\mathbf{x}_{i+}) = +1 & \text{if } \mathbf{x}_{i+} \in \mathcal{X}^{(0)}, \\ \text{no label is assigned} & \text{ortherwise.} \end{cases} \tag{13}$$

- INITIALIZATION:
  - define a regular grid of n_0 points $\{\mathbf{x}_i\},\ i = 1, \dots, n_0$ over Ω where f is evaluated $\mathcal{X}^{(0)} \longleftarrow \{\mathbf{x}_1, \dots, \mathbf{x}_{n_0}\}$,
  - build the Delaunay triangulation of Ω, it contains t_0 elements $\mathbf{T}_j^{(0)},\ j = 1, \dots, t_0$ $\mathcal{T}^{(0)} \longleftarrow \{\mathbf{T}_1^{(0)}, \dots, \mathbf{T}_{t_0}^{(0)}\}$,
  - set the iteration counter $k \longleftarrow 0$.
- MESH ANALYSIS:
  - $\forall j \in [\![1, t_k]\!]$, compute $\mathbf{y}_j^{(k)}$ as the barycenter of $\mathbf{T}_j^{(k)}$,
  - $\forall j \in [\![1, t_k]\!]$, compute $\mathcal{L}_{\mathcal{M}} f(\mathbf{y}_j^{(k)})$ as described in Sec. 3.2.1,
  - if $k = 0$, compute $\mathcal{L}_{\mathcal{M}} f_{\max} = \max_{j \in [\![1, t_0]\!]}(\mathcal{L}_{\mathcal{M}} f(\mathbf{y}_j^{(0)}))$,
  - define the set of suitable indices $\mathcal{I}^{(k)} = [\![1, t_k]\!]$.
- IDENTIFICATION OF A SUITABLE ELEMENT:
  - find $i \in \mathcal{I}^{(k)}$ such that $\mathcal{L}_{\mathcal{M}} f(\mathbf{y}_i^{(k)}) = \max_{j \in \mathcal{I}^{(k)}}(\mathcal{L}_{\mathcal{M}} f(\mathbf{y}_j^{(k)}))$, vertices of the element $\mathbf{T}_i^{(k)}$ are denoted $\{\mathbf{x}_{i_1}, \mathbf{x}_{i_2}, \mathbf{x}_{i_3}\}$ with $i_1, i_2, i_3 \in [\![1, n_k]\!]$,
  - if $\mathcal{L}_{\mathcal{M}} f(\mathbf{y}_i^{(k)}) \leq \lambda_L \mathcal{L}_{\mathcal{M}} f_{\max}$, a stopping criterion is met: end of the procedure and $k_{\text{ed}} \longleftarrow k$,
  - find $i^+, i^- \in \{i_1, i_2, i_3\}$ such that: $f(\mathbf{x}_{i^+}) = \max_{\{i_1, i_2, i_3\}} f(\mathbf{x}_i)$ and $f(\mathbf{x}_{i^-}) = \min_{\{i_1, i_2, i_3\}} f(\mathbf{x}_i)$,
  - compute the new point $\mathbf{x}_{n_0+k+1} = (\mathbf{x}_{i^+} + \mathbf{x}_{i^-})/2$,
  - if $\exists q \in [\![1, n_k]\!], \|\mathbf{x}_q - \mathbf{x}_{n_0+k+1}\|_2 \leq \lambda_{\text{dist}}$ then $\mathcal{I}^{(k)} = \mathcal{I}^{(k)} \backslash \{i\}$,
    - if $\mathcal{I}^{(k)} = \{\emptyset\}$ a stopping criterion is met: end of the procedure and $k_{\text{ed}} \longleftarrow k$,
    - otherwise, go back to IDENTIFICATION OF A SUITABLE ELEMENT,
  - otherwise, add point $\mathbf{x}_{n_0+k+1}$ to the set of points $\mathcal{X}^{(k)}$: $\mathcal{X}^{(k+1)} \longleftarrow \mathcal{X}^{(k)} \cup \{\mathbf{x}_{n_0+k+1}\}$.
- REMESHING:
  - compute $\mathcal{T}^{(k+1)}$ by means of a Delaunay triangulation based on $\mathcal{X}^{(k+1)}$,
  - increment the iteration counter: $k \longleftarrow k + 1$,
  - if $k < k_{\max}$, go to MESH ANALYSIS,
  - otherwise, end the procedure and $k_{\text{ed}} \longleftarrow k_{\max}$.

Figure 6. Iterative edge detection algorithm.

The label of the newly defined point $\mathbf{x}_{n_0+k+1} = \mathbf{x}_{n_{k+1}}$ is then assigned depending on the following criterion:

$$\begin{cases} \text{label}(\mathbf{x}_{n_{k+1}}) = -1 & \text{if } |f(\mathbf{x}_{n_{k+1}}) - f(\mathbf{x}_{i-})| < \frac{1}{2}(1-\gamma)|f(\mathbf{x}_{i+}) - f(\mathbf{x}_{i-})|, \\ \text{label}(\mathbf{x}_{n_{k+1}}) = +1 & \text{if } |f(\mathbf{x}_{n_{k+1}}) - f(\mathbf{x}_{i+})| < \frac{1}{2}(1-\gamma)|f(\mathbf{x}_{i+}) - f(\mathbf{x}_{i-})|, \\ \text{no label is assigned to } \mathbf{x}_{n_{k+1}} & \text{ortherwise,} \end{cases} \tag{14}$$

with $\gamma \in [0, 1]$. Parameter γ prevents the labeling of areas of high variations of f. In the end, the proposed iterative algorithm relies on four numerical parameters: λ_L, λ_{dist}, $k_{\max}$ and γ.

3.2.4 Area of discontinuity

At the end of the iterative edge detection procedure, the mesh of Ω has been refined in the vicinity of the predicted discontinuities. At this stage, each element $\mathbf{T}_j^{(k)} \in \mathcal{T}^{(k)}$ is sorted depending on the labels assigned to its vertices. The elements $\mathbf{T}_j^{(k)} \in \mathcal{T}^{(k)}$ with at least one vertex of class $+1$ and one vertex of class -1 are then sorted as:

$$\exists\ (l, m) \in \{j_1, j_2, j_3\}, \text{label}(\mathbf{x}_l) = -1 \text{ and } \text{label}(\mathbf{x}_m) = +1. \tag{15}$$

To target only the elements containing discontinuities, elements are also selected based on their jump value such that it verifies the following condition for the barycenter $\mathbf{y}_j^{(k)}$ of element $\mathbf{T}_j^{(k)} \in \mathcal{T}^{(k)}$:

$$\mathcal{L}_{\mathcal{M}} f(\mathbf{y}_j^{(k)}) \geq \mathcal{L}_{\mathcal{M}} f_{\min}, \tag{16}$$

where $\mathcal{L}_{\mathcal{M}} f_{\min} = \min_{k \in [\![0, k_{\text{ed}}]\!]} (\mathcal{L}_{\mathcal{M}} f(\mathbf{y}_i^{(k)})), i \in \mathcal{I}^{(k)}$, is the smallest value of $\mathcal{L}_{\mathcal{M}} f(\mathbf{y}_i^{(k)})$ obtained during the iterative algorithm. The set $\mathcal{E}^{(k)}$ including all elements containing discontinuities is thus defined by the elements $\mathbf{T}_j^{(k)} \in \mathcal{T}^{(k)}$ satisfying Eqs. (15) and (16). Elements of $\mathcal{E}^{(k)}$ are then separated in n_d subsets $\mathcal{E}_p^{(k)}$, $p = 1, \ldots, n_d$, such that $\mathcal{E}_p^{(k)}$ only contains elements of $\mathcal{E}^{(k)}$ having at least one vertex in common following the procedure described in Fig. 7. The number n_d of subsets corresponds to the number of discontinuities detected by the iterative edge detection procedure over the random space. For the following steps, vertices of elements in each subset $\mathcal{E}_p^{(k)}$ are sorted depending on their label. Two subsets of points are thus created $\mathcal{G}_{p+}^{(k)}$ and $\mathcal{G}_{p-}^{(k)}$, for each vertex $\mathbf{x}$ of all elements $\mathbf{T}_j^{(k)} \in \mathcal{E}_p^{(k)}$, such that:

$$\begin{cases} \mathbf{x} \in \mathcal{G}_{p+}^{(k)} & \Leftrightarrow \quad \text{label}(\mathbf{x}) = +1, \\ \mathbf{x} \in \mathcal{G}_{p-}^{(k)} & \Leftrightarrow \quad \text{label}(\mathbf{x}) = -1. \end{cases} \tag{17}$$

In order to assign all vertices of the elements of $\mathcal{E}_p^{(k)}$, if a vertex has the default label 0, then its label becomes same as the vertex of the elements of $\mathcal{E}_p^{(k)}$ in its close vicinity whose label is different from 0 and whose evaluation of f is closest to that of point to be labelled. Eq. (17) can then be applied.

- INITIALIZATION:
  - identify $\mathcal{E}^{(k)}$, set $\mathcal{F}^{(k)} \longleftarrow \mathcal{E}^{(k)}$,
  - set the discontinuity index $p \longleftarrow 0$.
- SELECTION OF A DISCONTINUITY:
  - increment the discontinuity index: $p \longleftarrow p + 1$,
  - select one element $\mathbf{T}_j^{(k)}$ in $\mathcal{F}^{(k)}$
    $\mathcal{F}^{(k)} \longleftarrow \mathcal{F}^{(k)} \setminus \{\mathbf{T}_j^{(k)}\}$ and $\mathcal{E}_p^{(k)} \longleftarrow \{\mathbf{T}_j^{(k)}\}$,
  - identify neighboring elements of $\mathbf{T}_j^{(k)}$:
    $\mathcal{V} \longleftarrow \{\mathbf{T}_i^{(k)} \in \mathcal{F}^{(k)} | \mathbf{T}_j^{(k)} \bigcap \mathbf{T}_i^{(k)} \neq \{\emptyset\}\}$.
- CONCATENATION OF THE SET $\mathcal{E}_p^{(k)}$:
  - concatenate $\mathcal{V}$ and $\mathcal{E}_p^{(k)}$:
    $\mathcal{E}_p^{(k)} \longleftarrow \mathcal{E}_p^{(k)} \bigcup \mathcal{V}$ and $\mathcal{F}^{(k)} \longleftarrow \mathcal{F}^{(k)} \setminus \mathcal{V}$,
  - update the set of neighboring elements:
    $\mathcal{V} \longleftarrow \{\mathbf{T}_i^{(k)} \in \mathcal{F}^{(k)} | \exists \mathbf{T}_n^{(k)} \in \mathcal{V},\ \mathbf{T}_n^{(k)} \bigcap \mathbf{T}_i^{(k)} \neq \{\emptyset\}\}$,
  - if $\mathcal{V} = \{\emptyset\}$, go to ITERATION,
  - otherwise, go back to CONCATENATION OF THE SET $\mathcal{E}_p^{(k)}$.
- ITERATION:
  - if $\mathcal{F}^{(k)} \neq \{\emptyset\}$, go to SELECTION OF A DISCONTINUITY,
  - otherwise, end the procedure and $n_d \longleftarrow p$.

Figure 7. Algorithm for the definition of the set $\mathcal{E}_p^{(k)}$.

An illustration of the application of the proposed algorithm to the function $\mathcal{D}(k, F)$ introduced above on the mesh depicted in Fig. 5 is shown in Fig. 8. For this application, a single discontinuity ($n_d = 1$) is predicted over the random space.

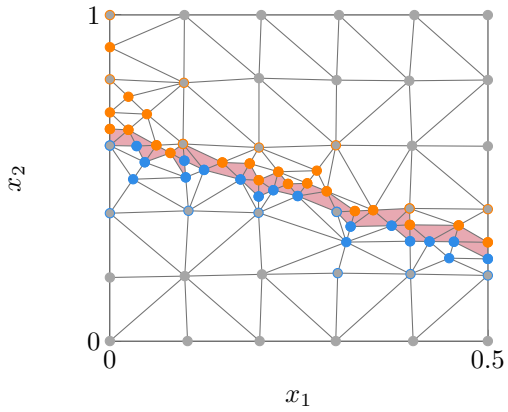

Figure 8. Result of the iterative edge detection procedure on the Duffing oscillator: point of edge detection labeled -1 (●) and $+1$ (●), identification of the area of discontinuity (■), with the points of initial mesh (●), labeled $+1$ (●) or -1 (●).

3.3 Discontinuity description with support vector machine

For each area of discontinuity, support vector machine (SVM) is used to separate points of $\mathcal{G}_{p+}^{(k)}$ and $\mathcal{G}_{p-}^{(k)}$. The SVM steps are not detailed in this article for the sake of conciseness, the reader is referred to the description of C-Support Vector Classification widely detailed in the literature [31, 32, 33]. The result of the application of SVM is a B-spline (–●–), see Fig. 9. In this figure, points of $\mathcal{G}_{p+}^{(k)} \bigcup \mathcal{G}_{p-}^{(k)}$ are split into a training set (●) and (●), and a test set (○) and (○), before obtaining the the classification boundary represented by the B-spline (–●–). The definition of the test and training sets from the points of $\mathcal{G}_{p+}^{(k)} \bigcup \mathcal{G}_{p-}^{(k)}$ are detailed in the next subsection. The accuracy of the

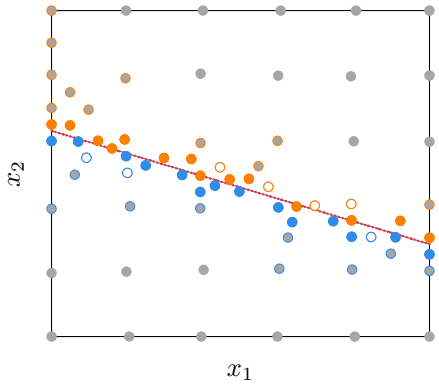

Figure 9. Application of SVM: training (●) (●) and test (○) (○) sets to obtain the classification boundary (–●–), with the points of initial mesh or edge detection (●), labeled $+1$ (●) or -1 (●).

discontinuity is quantified by a scalar value s_{svm} computed as follows:

$$s_{\text{svm}}(\mathcal{G}_{p+}^{(k)} \bigcup \mathcal{G}_{p-}^{(k)}) = \frac{\#\text{correctly predicted data}}{\#\text{testing data}} \times 100 \quad [\%], \tag{18}$$

where the testing data consists of the unselected points of $\mathcal{G}_{p+}^{(k)} \bigcup \mathcal{G}_{p-}^{(k)}$ in the the training data.

3.4 Step 2: localized mesh refinement

The localized mesh refinement step intends to increase the fidelity of the B-spline obtained by means of the aforementioned SVM procedure at the end of the iterative edge detection step. Building on a previously published

unstructured approach [19], the proposed algorithm prioritarily focuses on the least dense areas all along the discontinuity. As detailed in Fig. 10, for each of the p discontinuities, the algorithm relies on a discretization of the B-spline in n_u points whose closest counterparts in $\mathcal{G}_{p+}^{(k)} \bigcup \mathcal{G}_{p-}^{(k)}$ are identified at each iteration. The vicinity of the point $\mathbf{u}_{i_0}$ of the B-spline for which this counterpart—denoted $\mathbf{x}_{j_0}$ in Fig. 10—is the furthest is where a point is added. By default, the added point $\mathbf{x}_{n_0+k+1}$ is located half way between $\mathbf{u}_{i_0}$ and $\mathbf{x}_{j_0}$. However, in order to avoid point clustering, it is checked that there is no other point of $\mathcal{G}_{p+}^{(k)} \bigcup \mathcal{G}_{p-}^{(k)}$ close to $\mathbf{x}_{n_0+k+1}$: should a point of $\mathcal{G}_{p+}^{(k)} \bigcup \mathcal{G}_{p-}^{(k)}$ be found within a circle around $\mathbf{x}_{n_0+k+1}$, the ORTHOGONAL SEARCH procedure is activated, see Fig. 11. Contrary to

- INITIALIZATION:
  - set the iteration counter $k \longleftarrow k_{\text{ed}}$,
  - set $n_p^{(k)} \longleftarrow \#\left(\mathcal{G}_{p+}^{(k)} \bigcup \mathcal{G}_{p-}^{(k)}\right)$.
- DISCONTINUITY MODELING:
  - compute a set of points along the spline obtained with Sec. 3.3: $\mathcal{U}_p^{(k)} \longleftarrow \{\mathbf{u}_i^{(k)}, i \in [\![0, n_u]\!]\}$,
  - compute the distance matrix $\mathbf{D}$: $\forall \mathbf{u}_i^{(k)} \in \mathcal{U}_p^{(k)}, \forall \mathbf{x}_j \in \mathcal{G}_{p+}^{(k)} \bigcup \mathcal{G}_{p-}^{(k)}, D_{ji} = \|\mathbf{x}_j - \mathbf{u}_i\|_2$,
  - define the set $\mathcal{J}_p^{(k)} = \{\arg\min_{j \in [\![1, n_p^{(k)}]\!]} D_{ji}, \forall i \in [\![0, n_u]\!]\}$,
- IDENTIFICATION OF A SUITABLE POINT:
  - find $D_{j_0 i_0} = \max_{j \in \mathcal{J}_p^{(k)}, i \in [\![0, n_u]\!]}(D_{ji})$ and compute $s_{\text{svm}}(\mathcal{G}_{p+}^{(k)} \bigcup \mathcal{G}_{p-}^{(k)})$ with Eq. (18),
  - if $D_{j_0 i_0} \leq \lambda_D$ and $s_{\text{svm}}(\mathcal{G}_{p+}^{(k)} \bigcup \mathcal{G}_{p-}^{(k)}) \geq \lambda_{\text{svm}}$, a the stopping criterion is met $k \longleftarrow k_{\text{mr}}$,
  - otherwise compute the new point $\mathbf{x}_{n_0+k+1} = \frac{(\mathbf{x}_{j_0} + \mathbf{u}_{i_0})}{2}$,
  - if $\exists \mathbf{x}_j \in \mathcal{G}_{p+}^{(k)} \bigcup \mathcal{G}_{p-}^{(k)}, \|\mathbf{x}_{n_0+k+1} - \mathbf{x}_j\|_2 \leq 0.25 D_{j_0 i_0}$ then ORTHOGONAL SEARCH
  - otherwise, go to LABELING.
- LABELING:
  - find $\mathbf{x}_{j^+} = \min_{\mathbf{x}_j \in \mathcal{G}_{p+}^{(k)}} \|\mathbf{x}_j - \mathbf{x}_{n_0+k+1}\|_2$ and $\mathbf{x}_{j^-} = \min_{\mathbf{x}_j \in \mathcal{G}_{p-}^{(k)}} \|\mathbf{x}_j - \mathbf{x}_{n_0+k+1}\|_2$,
  - if $|f(\mathbf{x}_{j^+}) - f(\mathbf{x}_{n_0+k+1})| < |f(\mathbf{x}_{j^-}) - f(\mathbf{x}_{n_0+k+1})|$, then $\mathcal{G}_{p+}^{(k+1)} \longleftarrow \mathcal{G}_{p+}^{(k)} \cup \{\mathbf{x}_{n_0+k+1}\}$,
  - otherwise: $\mathcal{G}_{p-}^{(k+1)} \longleftarrow \mathcal{G}_{p-}^{(k)} \cup \{\mathbf{x}_{n_0+k+1}\}$,
  - go to UPDATE
- UPDATE:
  - increment the iteration counter: $k \longleftarrow k+1$,
  - if $k < k_{\max}$, go to DISCONTINUITY MODELING,
  - otherwise, $k_{\text{mr}} \longleftarrow k_{\max}$ and end the procedure.

Figure 10. Localized mesh refinement for the p-th discontinuity.

the iterative edge detection procedure, point labeling is here embedded within the localized mesh refinement as it is necessary to identify if the added point belongs to $\mathcal{G}_{p-}^{(k)}$ or $\mathcal{G}_{p+}^{(k)}$.

The localized mesh refinement procedure yields a more uniformly spread set of labeled points around the discontinuity thus minimizing the discrepancy between the B-spline and the actual discontinuity. Beside of a maximum number of evaluations $k_{\max}$, there are two stopping criteria related to: (1) a minimal distance λ_D between $\mathbf{u}_{i_0}$ and $\mathbf{x}_{j_0}$ to prevent excessive mesh refinement similarly to the original algorithm [19], and (2) a threshold λ_{svm} above which the accuracy of the SVM is considered sufficient.

For the sake of clarity, key aspects of the proposed algorithm are illustrated in Fig. 12, including the conditional ORTHOGONAL SEARCH procedure, for the Duffing reference system. At the end of the localized mesh refinement procedure, the number of iterations k_{mr} is stored and the set of all points evaluated in the proposed automated

- ORTHOGONAL SEARCH, see Fig. 12(b)
  - compute the tangent vector $\mathbf{t}_{i_0}$ to the spline at $\mathbf{u}_{i_0}$ and define $\mathbf{x}^{\bullet}_{n_0+k+1}$ such that:,

$$\begin{cases} \left\|\mathbf{x}^{\bullet}_{n_0+k+1} - \mathbf{x}_{n_0+k+1}\right\|_2 = \left\|\mathbf{x}_{j_0} - \mathbf{x}_{n_0+k+1}\right\|_2, \\ (\mathbf{x}^{\bullet}_{n_0+k+1} - \mathbf{x}_{n_0+k+1}) \cdot (\mathbf{x}_{j_0} - \mathbf{x}_{n_0+k+1}) = 0, \\ \text{sign}((\mathbf{x}^{\bullet}_{n_0+k+1} - \mathbf{x}_{n_0+k+1}) \cdot \mathbf{t}_{i_0}) = \bullet\, \text{sign}((\mathbf{x}_{j_0} - \mathbf{x}_{n_0+k+1}) \cdot \mathbf{t}_{i_0}), \end{cases} \quad \text{where } \bullet = \{+, -\},$$

  - if $\nexists \mathbf{x}_j \in \mathcal{G}^{(k)}_{p+} \bigcup \mathcal{G}^{(k)}_{p-}, \left\|\mathbf{x}^{-}_{n_0+k+1} - \mathbf{x}_j\right\|_2 \leq 0.25 D_{j_0 i_0}$ and $\mathbf{x}^{-}_{n_0+k+1} \in \Omega$, then $\mathbf{x}_{n_0+k+1} = \mathbf{x}^{-}_{n_0+k+1}$, and go to LABELING,
  - otherwise, if $\nexists \mathbf{x}_j \in \mathcal{G}^{(k)}_{p+} \bigcup \mathcal{G}^{(k)}_{p-}, \left\|\mathbf{x}^{+}_{n_0+k+1} - \mathbf{x}_j\right\|_2 \leq 0.25 D_{j_0 i_0}$ and $\mathbf{x}^{+}_{n_0+k+1} \in \Omega$, then $\mathbf{x}_{n_0+k+1} = \mathbf{x}^{+}_{n_0+k+1}$, and go to LABELING,
  - otherwise, $\mathcal{J}^{(k)}_p = \mathcal{J}^{(k)}_p \backslash \{j_0\}$, if $\mathcal{J}^{(k)}_p = \emptyset$, then end the procedure $k \longleftarrow k_{\text{mr}}$,
  - go to IDENTIFICATION OF A SUITABLE POINT.

Figure 11. Details of the ORTHOGONAL SEARCH procedure.

detection of discontinuities is noted $X^{(k_{\text{ad}})}$ of size $n_{k_{\text{ad}}}$.

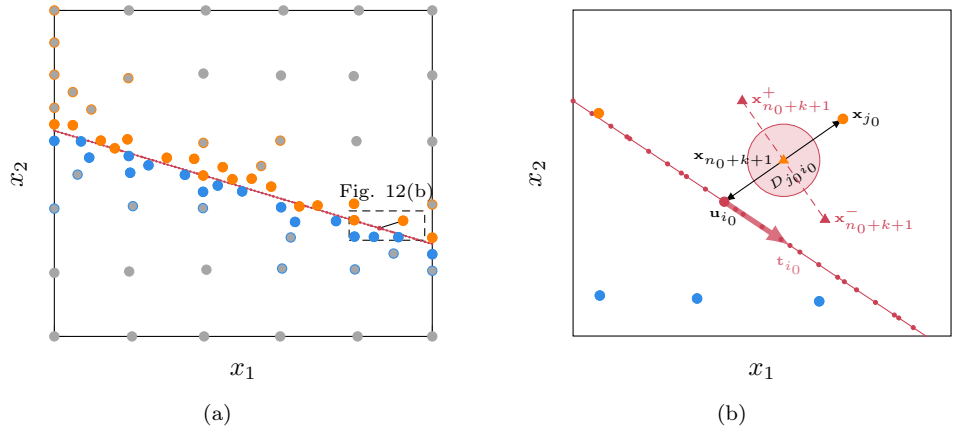

Figure 12. First step of the localized mesh refinement procedure: (a) view over Ω; (b) zoom and depiction of the possible point of the ORTHOGONAL SEARCH procedure from points of initial mesh or edge detection (●), labeled +1 (●) or -1 (●), points of $\mathcal{G}^{(k)}_{p+}$ (●) and $\mathcal{G}^{(k)}_{p-}$ (●), spline (●—●) and new point $\mathbf{x}_{n_0+k+1}$ (▲).

3.5 Application to academic systems

In this subsection, the proposed automated detection of discontinuities is applied on three distinct academic systems, introduced in subsection 2.4, in order to illustrate its robustness. The considered numerical parameters, obtained after a sensitivity analysis not detailed here for the sake of brevity, are listed in Tab. 2. For all the presented test cases, the initial mesh is built from 36 points and a maximum number of evaluations $k_{\max} = 164$ is imposed so that the maximum number of evaluations of the system's response is 200.

The discontinuity detection is first applied on the Duffing oscillator, see Fig. 1. Following the iterative edge detection and the localized mesh refinement procedures, the detected discontinuity (●—●) is depicted in Fig. 13(a). An approximation of the discontinuity (—) based on a brute force evaluation of the system's response surface using a regular grid of 100 × 100 points over Ω is also depicted in order to assess the accuracy of the automated detection

$k_{\max}$	γ	λ_{dist}	λ_L	λ_D	λ_{svm}
164	0.2	0.25	0.2	0.1	0.8

Table 2. Numerical parameters used for the academic systems.

procedure. The detected discontinuity shown in Fig. 13(a) yields good agreement with the reference discontinuity. For this first test case, using the numerical parameters given in Tab. 2, the total number of evaluations of the system's response is 85, split as follows: 36 evaluations for the initial mesh, 39 evaluations made during the iterative edge detection step and 10 additional evaluations during the localized mesh refinement step.

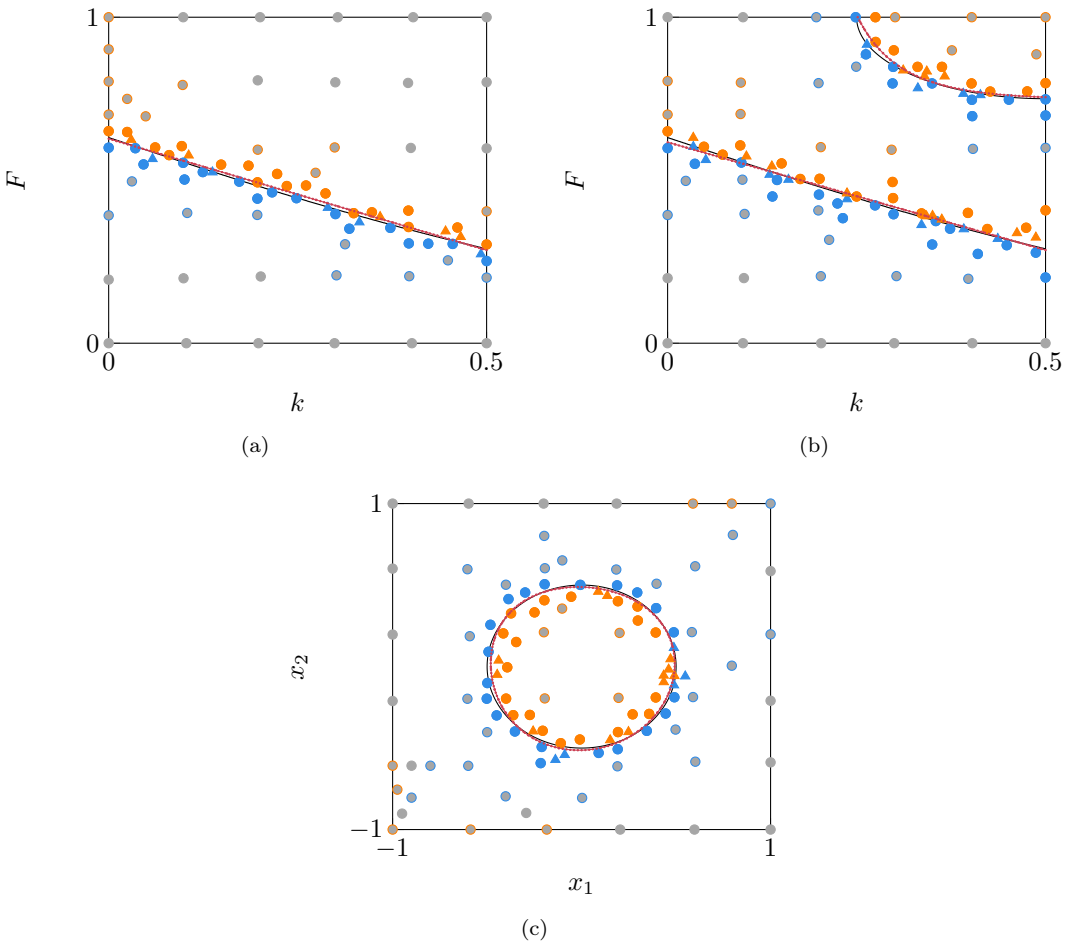

Figure 13. Automated discontinuity detection for academic systems: (a) Duffing oscillator; (b) Duffing oscillator with added discontinuity; (c) circular discontinuity [22] from initial mesh (●), points of $\mathcal{G}_{p+}^{(k_{\text{ed}})}$ (●) and $\mathcal{G}_{p-}^{(k_{\text{ed}})}$ (●), points added during the localized mesh refinement step (▲) with label +1 (○) or −1 (○). Detected (–●–) and reference (—) discontinuities.

The second test case relies on the Duffing oscillator with added discontinuity. The second discontinuity is imposed on the response surface as shown in Fig. 4(a). The two discontinuities are correctly identified by the proposed procedure, see Fig. 13(b) where the detected discontinuities (–●–) are superimposed with a brute force approximation (—) obtained with regular 100×100 grid over Ω. A total number of 111 evaluations of the system's

response are here required: 36 evaluations for the initial mesh, 50 evaluations made during the iterative edge detection step and 25 additional evaluations during the localized mesh refinement step.

Finally, the last test case relies on a benchmark function previously used in the literature [22], for which the discontinuity has a perfectly circular shape (—). As shown in Fig. 13(c), the proposed methodology yields an accurate approximation of the discontinuity (-●-) using 112 evaluations of the system's response: 36 evaluations for the initial mesh, 59 evaluations made during the iterative edge detection step and 17 additional evaluations during the localized mesh refinement step.

4 Approximation of the response surface

Once the discontinuities of the response surface have been detected, it becomes possible to decompose the random space into a set of relevant subdomains well-suited for the application of gPCE. In particular, in order to avoid spurious oscillations of the approximated response surface shown in Figs. 2 and 3, boundaries of the subdomains are here defined so that they are coincident with the detected discontinuities. This allows to define an optimal number of subdomains over which the system's response is smooth thus lowering the computational cost associated with the evaluation of the system's response surface while preventing spurious oscillations.

In the following subsections, the proposed approach is detailed from a theoretical standpoint: key notations related to the domain decomposition, fundamental aspects of the mapping between random spaces as well as the management of the Design of Experiments (DoE) are each presented in a dedicated subsection.

4.1 Domain decomposition

One may distinguish different types of discontinuities depending on their number of intersections with the boundary $\partial\Omega$ of the random space Ω. If a discontinuity has two intersections with $\partial\Omega$, which is the case for the Duffing oscillator, see Fig. 14(a), it splits the random space into two subdomains Ω_1 and Ω_2, see Fig. 14(c), that may be directly considered for the next steps of the proposed methodology. However, in the case where the discontinuity has only one (or possibly no) intersection with $\partial\Omega$ as depicted in Fig. 14(b), a specific post-processing step is required to define the subdomains. As an example, one may consider extending the mathematical definition of the discontinuity until it intersects $\partial\Omega$ as depicted in Fig. 14(d).

In the following, it is assumed that the random space Ω is decomposed into N non-overlapping subdomains such as:

$$\begin{cases} \Omega = \bigcup_{i=1}^{N} \Omega_i, \\ \forall i, j \in [\![1, N]\!], i \neq j \Leftrightarrow \ \Omega_i \cap \Omega_j = \emptyset. \end{cases} \tag{19}$$

A versatile representation is considered for the boundaries of the subdomain Ω_i that are simply assumed to be parametric curves denoted $\mathbf{s}^s(\eta), \mathbf{s}^n(\eta), \mathbf{s}^w(\mu)$ and $\mathbf{s}^e(\mu)$, where the variable $[\eta, \mu]$ is defined on the parametric space $[0, 1]^2$. The output of each parametric curves is defined on the subdomain Ω_i. To better distinguish the two directions of the subdomain, the notation s_k is introduced with $k = \{1, 2\}$ for any parametric curves $\mathbf{s}$.

4.2 Key equations of gPCE

First introduced by Wiener [5], polynomial chaos expansion is based on an expansion of a stochastic system's response, which is assumed to be of finite variance, into a series of orthogonal polynomials. Generalized PCE refers to the generalization of PCE to a large variety of probability distributions through the Askey scheme [10]. Following the Askey scheme, a transformation T defined by:

$$\begin{aligned} T\colon [-1, 1]^2 &\to \Omega, \\ \boldsymbol{\xi} &\mapsto \mathbf{x} = T(\boldsymbol{\xi}), \end{aligned} \tag{20}$$

is applied for the change of the variable $\mathbf{x}$ into a centered random variable $\boldsymbol{\xi}$. Considering a finite number of terms in the expansion, the approximation of the system's response Y by the gPCE is written as:

$$Y(\boldsymbol{\xi}) \approx \sum_{j=0}^{p} a_j \Psi_j(\boldsymbol{\xi}), \tag{21}$$

where a_j and Ψ_j are the gPCE coefficients to be determined and the gPCE basis, respectively. In this paper, the random variables follow a uniform distribution, accordingly the gPCE basis is composed of Legendre polynomials in agreement with the Askey scheme. The two-dimensional orthogonal polynomials Ψ_j are limited to degrees lower or equal to a maximum degree q. The gPCE basis is thus composed of:

$$p + 1 = \frac{(q+2)!}{q!2!}, \tag{22}$$

terms. The gPCE coefficients a_j may be calculated by an intrusive method, such as Galerkin methods [3, 11], or a non-intrusive method, through projection or regression methods [12, 34]. In this paper, a regression method, based

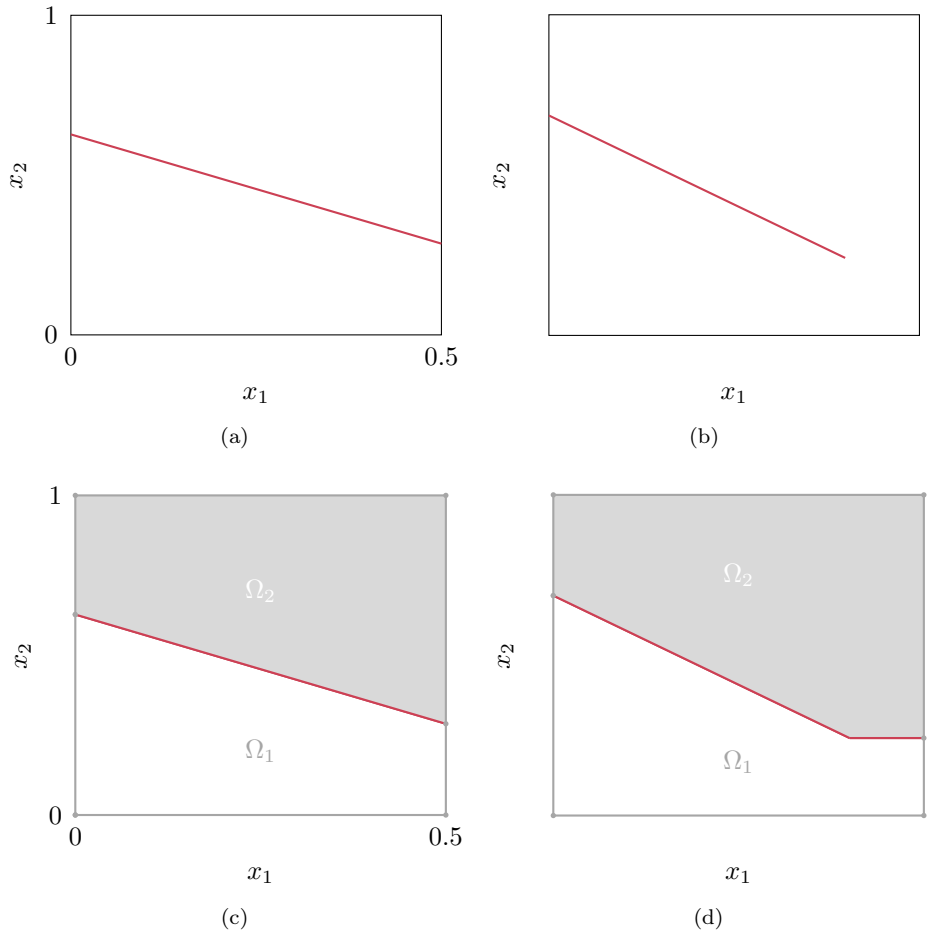

Figure 14. Domain decomposition for different types of discontinuities: (a) discontinuity detected for the Duffing oscillator; (b) example of discontinuity with a single intersection with $\partial\Omega$; (c) domain decomposition for the Duffing oscillator; (d) domain decomposition for the example of discontinuity with a single intersection with $\partial\Omega$.

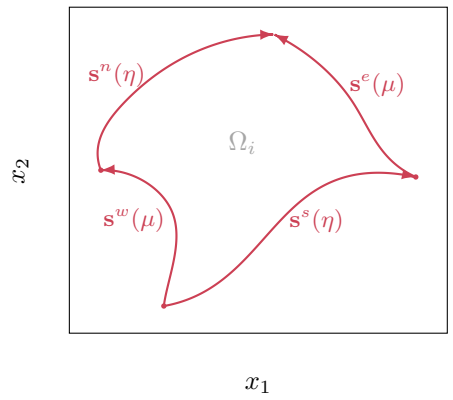

Figure 15. Subdomain Ω_i bounded by four parametric curves (➔).

on least squares approach, is selected as it is well-suited for many types of systems [1, 8]. Coefficients a_j are then obtained from solving the linear system [7]:

$$\begin{bmatrix} \sum_{i=1}^{n} \Psi_0(\tilde{\boldsymbol{\xi}}^{(i)})\Psi_0(\tilde{\boldsymbol{\xi}}^{(i)}) & \cdots & \sum_{i=1}^{n} \Psi_0(\tilde{\boldsymbol{\xi}}^{(i)})\Psi_p(\tilde{\boldsymbol{\xi}}^{(i)}) \\ \vdots & \ddots & \vdots \\ \sum_{i=1}^{n} \Psi_p(\tilde{\boldsymbol{\xi}}^{(i)})\Psi_0(\tilde{\boldsymbol{\xi}}^{(i)}) & \cdots & \sum_{i=1}^{n} \Psi_p(\tilde{\boldsymbol{\xi}}^{(i)})\Psi_p(\tilde{\boldsymbol{\xi}}^{(i)}) \end{bmatrix} \begin{bmatrix} a_0 \\ \vdots \\ a_p \end{bmatrix} = \begin{bmatrix} \sum_{i=1}^{n} Y(\tilde{\boldsymbol{\xi}}^{(i)})\Psi_0(\tilde{\boldsymbol{\xi}}^{(i)}) \\ \vdots \\ \sum_{i=1}^{n} Y(\tilde{\boldsymbol{\xi}}^{(i)})\Psi_p(\tilde{\boldsymbol{\xi}}^{(i)}) \end{bmatrix}, \tag{23}$$

where the n points $\tilde{\boldsymbol{\xi}}^{(i)}$ constitute the design of experiments on which the system's response $Y(\tilde{\boldsymbol{\xi}}^{(i)})$ is evaluated.

4.3 Application of gPCE on *ad-hoc* subdomains

In order to efficiently apply gPCE on the subdomain Ω_i depicted in Fig. 15, one must locally define the transformation T mentioned in Eq. (20) using a transformation T_i related to the subdomain Ω_i as follows:

$$\begin{aligned} T_i \colon [-1,1]^2 &\to \Omega_i, \\ \boldsymbol{\xi} &\mapsto \mathbf{x} = T_i(\boldsymbol{\xi}). \end{aligned} \tag{24}$$

It is thus necessary to map the subdomain Ω_i with the centered random space $[-1,1]^2$, as mentioned in Eq. (24). In this study, this mapping is made by means of a transfinite transformation which provides an explicit transformation adapted to parametric curves.

4.3.1 Transfinite mapping

The transfinite mapping [35, 36] is based on a transfinite interpolation defined by the boundaries of the subdomain Ω_i in order to map the parametric space $[0,1]^2$ into Ω_i. The transfinite mapping [37] yields a smooth mapping from a boundary to another, it is defined by a transfinite bilinear Lagrange interpolation obtained from a linear interpolation in η:

$$x_k^{sn} = (1-\mu)s_k^s(\eta) + \mu s_k^n(\eta), \quad k = \{1,2\}, \tag{25}$$

and a linear interpolation in μ:

$$x_k^{we} = (1-\eta)s_k^w(\mu) + \eta s_k^e(\mu), \quad k = \{1,2\}, \tag{26}$$

to which the bilinear surface is subtracted by:

$$\begin{bmatrix} x_1^{bil} \\ x_2^{bil} \end{bmatrix} = \begin{bmatrix} (1-\eta) & \eta \end{bmatrix} \begin{bmatrix} \mathbf{s}^s(0) & \mathbf{s}^n(0) \\ \mathbf{s}^s(1) & \mathbf{s}^n(1) \end{bmatrix} \begin{bmatrix} (1-\mu) \\ \mu \end{bmatrix}. \tag{27}$$

In summary, the transformation T_i used in Eq. (24) is here explicitly written as:

$$\begin{aligned} x_k =&(1-\mu)s_k^s(\eta) + \mu s_k^n(\eta) + (1-\eta)s_k^w(\mu) + \eta s_k^e(\mu) \\ &- (1-\eta)(1-\mu)s_k^s(0) - \mu(1-\eta)s_k^n(0) - (1-\mu)\eta s_k^s(1) - \eta\mu s_k^n(1), \quad k=\{1,2\}, \end{aligned} \tag{28}$$

where $\eta = (\xi_1+1)/2$ and $\mu = (\xi_2+1)/2$. In the context of gPCE, the transfinite transformation T_i easily allows to map the DoE from the centered random space to the random space so that the value of the system at each point of the DoE may be computed.

4.3.2 Design of experiments

In the context of the proposed methodology, defining the DoE in the centered random space must be prevented for the sake of computational efficacy. Indeed, for sophisticated nonlinear engineering systems, the evaluation of the system's response at each point of the DoE can be costly. This is the reason why it is here proposed to define the DoE based on points of $\mathcal{X}^{(k_{\text{ad}})}$ that also belong to the subdomain Ω_i, and for which the system's response has already been evaluated during the first phase: automated detection of discontinuities. The set of points in the DoE of the subdomain Ω_i, $i \in [\![1, N]\!]$, is defined as follows:

$$\mathcal{X}_i^{(k_{\text{ad}})} = \{\mathbf{x}_j \in \mathcal{X}^{(k_{\text{ad}})} \mid \mathbf{x}_j \in \Omega_i, \forall j \in [\![1, n_{k_{\text{ad}}}]\!]\}. \tag{29}$$

For each point of $\mathcal{X}_i^{(k_{\text{ad}})}$, it then becomes necessary to compute its coordinates in the centered random space through the inverse transformation T_i^{-1}.

Finding the coordinates in the centered random space $[-1,1]^2$ of a point $\mathbf{x}_j \in \mathcal{X}_i^{(k_{\text{ad}})}$ through the inverse transformation T_i^{-1} constitutes a nonlinear problem that may be solved iteratively using, for instance, a Newton-Raphson based procedure. Depending on the shape of the boundaries of the subdomain Ω_i, solving this problem may be numerically sensitive. In order to mitigate potential numerical issues at this stage, the nonlinear problem is solved sequentially over $\mathcal{X}_i^{(k_{\text{ad}})}$. For each point $\mathbf{x}_j$ the solution of the problem for its closest counterpart is here chosen as the initial guess used for the Newton-Raphson solver. The numerical cost of this algorithm is minimized thanks to a minimum spanning tree [38] built with the Kruskal algorithm [39] and a nearest neighbor search [40] in order to provide the sequence of nonlinear problems to solve and ensure an optimal selection of the initial guess. The starting point of this procedure is arbitrarily chosen at the center of the centered random space, see Fig. 16.

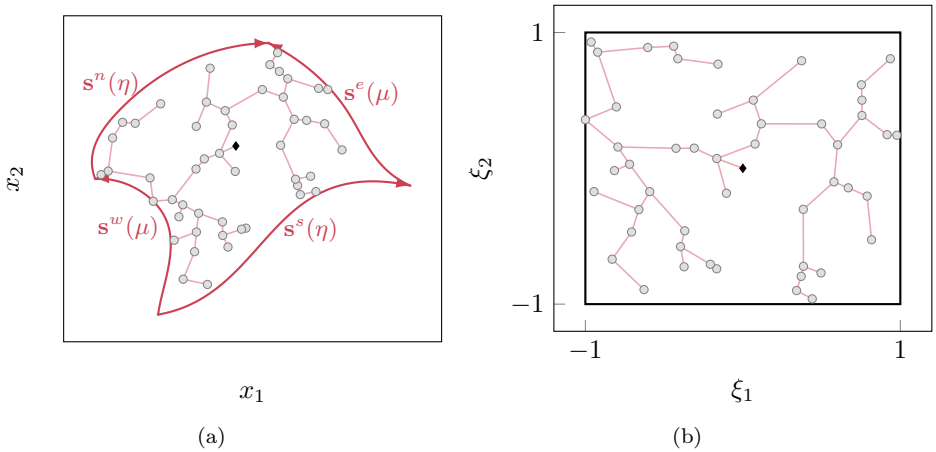

(a) (b)

Figure 16. Schematic representation of the inverse transformation with minimum spanning tree (—), starting point (⧫) and DoE (◎) based on: (a) points of $\mathcal{X}_i^{(k_{\text{ad}})}$ in subdomain Ω_i; (b) mapping of the points of $\mathcal{X}_i^{(k_{\text{ad}})}$ in the centered random space.

Since discontinuities are approximations, one must also ensure that the points of $\mathcal{X}_i^{(k_{\text{ad}})}$ are correctly on the right side of the discontinuity to avoid spurious oscillations in the gPC approximation as observed in Figs. 2 and 3.

The labels of the points of $\mathcal{X}_i^{(k_{\text{ad}})}$ are here checked in the vicinity of the detected discontinuity: if the label of the point and the one predicted by SVM are different, then the point is excluded from the DoE of the subdomain Ω_i.

4.3.3 Response surface of the system

The approximation of the response surface of the investigated system over Ω is obtained by reprensenting the response surface obtained by gPCE over each subdomain Ω_i determined in Eq. (19). In summary, the response surface approximation by the proposed ME-gPCE-based approach is a four step procedure:

1. decomposition of the random space Ω based on the detected discontinuities,
2. definition of the design of experiments on each subdomain according to section 4.3.2,
3. application of gPCE on each subdomain,
4. representation of the response surface obtained on each subdomain Ω_i.

4.4 Discussion on the proposed methodology

4.4.1 Limitations

The proposed methodology has been tested on a variety of configurations with both analytical functions and actual nonlinear engineering systems, as detailed in the next subsection. Based on these tests, the methodology appears robust and versatile. However, should a subdomain feature a high degree of non-convexity, it is possible that the transfinite mapping fail in the sense that points within the parametric space $[0,1]^2$ can be mapped outside the subdomain Ω_i. Strongly distorted boundaries of Ω_i would be required to observe this phenomenon but it remains a possibility and thus may call for a human intervention in the process for specific non-convex subdomains. In order to overcome this issue, the Winslow functional [41, 42] may be used, at the expense of a more sophisticated implementation.

4.4.2 Alternative

Through the transfinite mapping, the proposed methodology advantageously allows to use classical gPCE on each subdomain, each with a distinct centered random space. From a practical standpoint however, there exists an alternative that does not require the transfinite mapping. Indeed, in order to approximate the response surface over each subdomain, one could consider applying gPCE on the full random space while restricting the DoE to the considered subdomain only. By doing so for each subdomain, it is theoretically possible to obtain the response surface of the system over the full random space as a juxtaposition of cropped response surfaces obtained for each subdomain.

There is however a major drawback to this alternative. As a matter of fact, an accurate approximation of the response surface of the system requires, for each point where it is computed—a set potentially orders of magnitude larger than the number of points in the DoE—, to know exactly which subdomain it belongs to. While this may not be an issue far from the discontinuities, a nonlinear problem similar to the one solved in the proposed methodology with the inverse transform would have to be solved for each point close to the discontinuities. Failing to do so would unavoidably lead to an inaccurate approximation of the system's response close to its discontinuities, in direct contradiction with the emphasis put in their careful description.

4.4.3 Partial conclusion

Because the proposed methodology only relies on the transfinite mapping for points of the DoE, it is assumed to be an efficient strategy for the problem at hand. It also advantageously relies on a classical application of gPCE on each subdomain.

4.5 Application to academic systems

The proposed ME-gPCE-based approach is here applied on the three test cases previously introduced in subsection 2.4. For each application, the gPCE degree q is selected as the maximum value for which the basis size $p+1$ verifies that the number of points in DoE is higher or equal to $2(p+1)$.

Duffing oscillator: as shown in Fig. 17(a), the detected discontinuity (—) cuts the random space, thus separating two subdomains of Ω. From the 85 points evaluated, the design of experiments as defined in subsection 4.3.2

is respectively composed of 40 and 44 points for subdomains Ω_1 and Ω_2. A gPCE approximation is then performed on these two subdomains considering a degree of 4 and 5, respectively. The response obtained by the proposed methodology is depicted in Fig. 18(a). The Pearson correlation coefficient between this response and the reference response on the 10,000 reference samples is equal to 0.9961. The response obtained by the proposed methodology thus shows good agreement with the reference response while only 85 evaluations of the system's response are required.

Duffing oscillator with added discontinuity: the two detected discontinuities (—), plotted in Fig. 17(b), split the random space in three subdomains. The specificity of the subdomain Ω_3 is that the parametric curves $\mathbf{s}^n(\eta)$ is defined by the only coordinate $(0.5, 1)$ for all $\eta \in [0, 1]$. gPCE is applied with DoE composed of 40, 49 and 17 points on the subdomains Ω_1, Ω_2 and Ω_3, respectively. The proposed ME-gPCE approach yields the response surface plotted in Fig. 18(b) and the Pearson correlation coefficient obtained is equal to 0.9962. Good agreement between the obtained response and the reference response, shown in Fig. 4(a), is observed.

Circular discontinuity: [22] the detected discontinuity (—) is completely included in the random space Ω as shown in Fig. 17(c). The detected discontinuity is here splitted into four parametric curves so as to define the subdomain Ω_1, as well as the rest of Ω, decomposed into four subdomains. Thus, the decomposition of the random space represented in Fig. 17(c) features 5 subdomains. The 112 evaluations already performed are splitted according to the subdomains: the DoE are respectively composed of 35, 21, 18, 18 and 21 points. gPCE is applied with a degree 4 on subdomain Ω_1, degree 3 on subdomains Ω_2 and Ω_5, and degree 2 on subdomains Ω_3 and Ω_4. The response obtained by the proposed ME-gPCE approach is depicted in Fig. 18(c). The Pearson correlation coefficient obtained is equal to 0.9840. The obtained response surface shows a good agreement with the reference response over Ω. One may note that the quality of the approximation on subdomains Ω_2 and Ω_5 is lower, due to the lower value of the degree considered on these subdomains. Adding a few random points in the DoE over these subdomains would lead to better results.

In conclusion, in the three test cases, the response surface obtained by the proposed methodology is found to be accurate while requiring a limited number of evaluations of the system response.

5 Sensitivity analysis of key parameters

The influence of three parameters of interest are analyzed in this section: the initial mesh size n_0 and the two stopping criteria of the automatic detection of discontinuities, λ_{dist} and λ_D. The initial value of the parameters are detailed in Tab. 3. The analysis is performed for the Duffing oscillator with added discontinuity. The quantities of interest are (1) the computational cost of the methodology and (2) the accuracy of the approximation results. The latter is assessed by comparison to a reference response surface computed with 10,000 evaluations of the system's response. In the following, the degree of the polynomial chaos approximations on each subdomain is at most 4.

$k_{\max}$	n_0	γ	λ_{dist}	λ_L	λ_D	λ_{svm}
400	36	0.2	0.25	0.10	0.05	0.85

Table 3. Initial values of the discontinuity detection parameters.

5.1 Influence of the initial mesh size n_0

Considered values of the initial mesh size n_0 are $\sqrt{n_0} \in [\![4, 15]\!]$. The evolution of the number of evaluations and the correlation coefficient of the obtained results are plotted in Fig. 19. As observed in Fig. 19(a), the increase of the initial mesh size yields an increase in the total number of evaluations of the system and consequently of the computational costs of the methodology. More precisely, the increase of the initial mesh size n_0 leads to a finer triangulation implying a greater computational cost for the iterative edge detection step. The iterative edge detection step also provides a very satisfactory first estimate of the discontinuity with respect to the stopping criterion of the localized mesh refinement step which computational cost is then reduced. The results obtained by the methodology are compared in Fig. 19(b) using the correlation coefficient. The increase of the initial mesh size n_0 yields a small

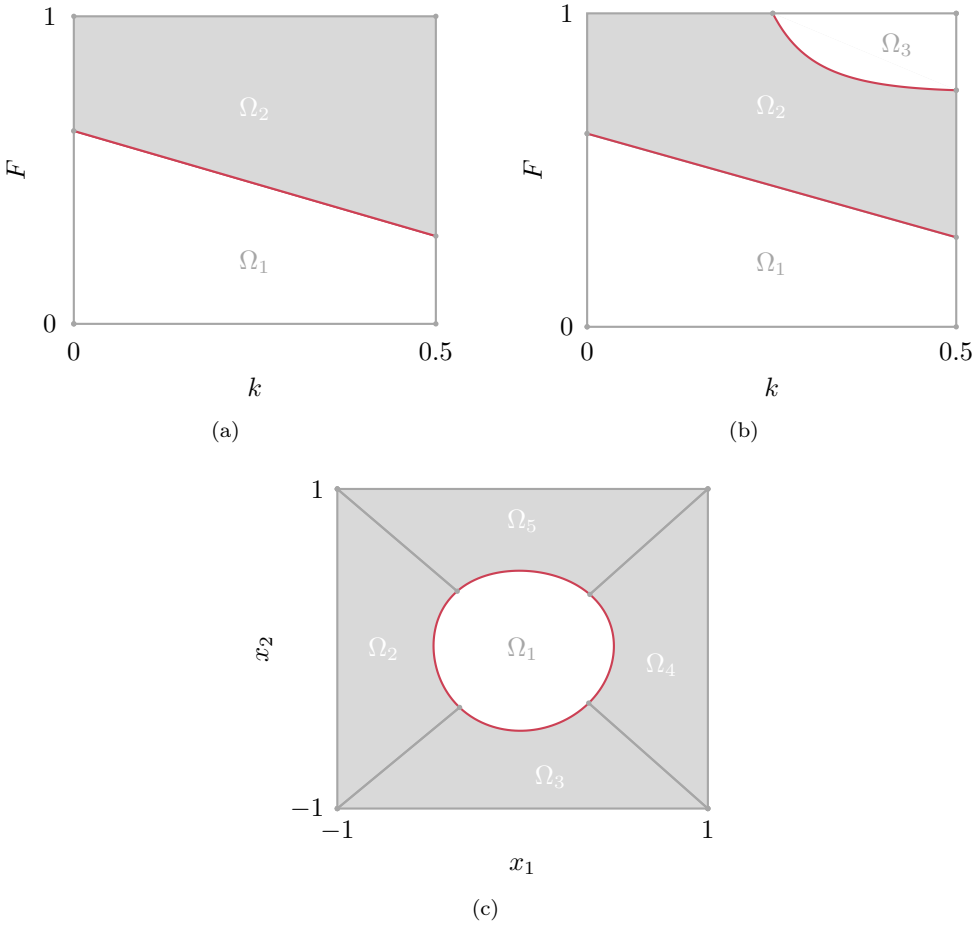

Figure 17. Domain decomposition for academic systems: (a) Duffing oscillator; (b) Duffing oscillator with added discontinuity; (c) circular discontinuity [22] from detected discontinuities (—).

increase of the correlation coefficient. All the Pearson correlation coefficients obtained are higher than 0.99 and reflect the good agreement with the reference response. The increase of the initial mesh size thus allows to improve the quality of the approximations obtained by the proposed methodology.

5.2 Influence of the λ_{dist} criterion of the iterative edge detection

The criterion of the iterative edge detection λ_{dist} is defined for values between 0 and 1. In this analysis, the upper bound of the tested values, set to 0.55, is the value for which the discontinuity location procedure did not converge due to a poor representation of the discontinuity zones for the initial 36 points mesh. The lower bound is set to 0.15 which is the minimum value for which the proposed methodology can obtain two discontinuities intersecting the boundary of the random space Ω.

Depending on the value of λ_{dist}, the number of evaluations and the correlation coefficient of the obtained results are depicted in Figs. 20(a) and 20(b) respectively. While several values of the criterion λ_{dist} are tested, the results obtained by the proposed methodology are similar: both in terms of computational costs with an average of 213 evaluations, and of accuracy with very high values of the Pearson correlation coefficients. With a similar computational cost between the simulations run for different values of λ_{dist}, it is noticeable that the split of the evaluations carried out between the two steps of the discontinuity detection procedure evolves according to the tested values. For a high λ_{dist} value, a high proportion of the evaluations are performed for localized mesh refinement (■).

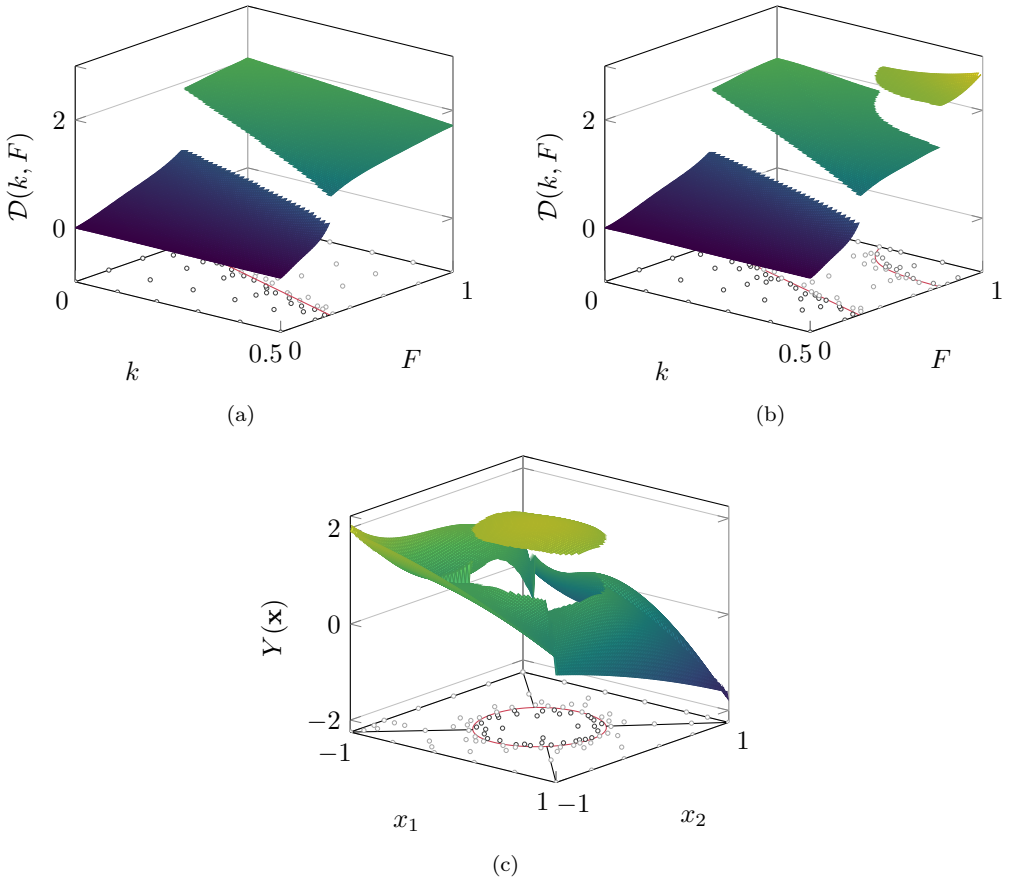

Figure 18. Response surface approximation by the proposed methodology for academic systems: (a) Duffing oscillator; (b) Duffing oscillator with added discontinuity; (c) circular discontinuity [22] from detected discontinuities (—) and points (○) (○) in DoE.

For a low λ_{dist} value, most of the evaluations are performed during the iterative edge detection (■). This observation highlights the complementarity of the two steps of the automated detection of discontinuities. In the end, the λ_{dist} criterion of the iterative edge detection does not influence the approximation quality nor the total computational cost of the methodology but mostly the distribution of the evaluations between the steps of the automated detection of discontinuities.

5.3 Influence of the point density criterion λ_D of the localized mesh refinement

The point density criterion λ_D of the localized mesh refinement, defined in $\mathbb{R}$, is studied here for values between 0.05 and 0.16. The maximal value is the upper bound where no points have been added in the localized mesh refinement. The minimal value is the lowest bound where the detection procedure converges to two discontinuities intersecting the boundary $\partial\Omega$ for the initial 36 points mesh.

The obtained results are depicted in Fig. 21, with (a) the number of evaluations and (b) the correlation coefficient. An increase in the number of evaluations is observed as λ_D decreases. Moreover, when this parameter decreases, the correlation coefficient increases. These observations highlight that the computational cost and the accuracy of the proposed approach both increase when the criterion λ_D decreases.

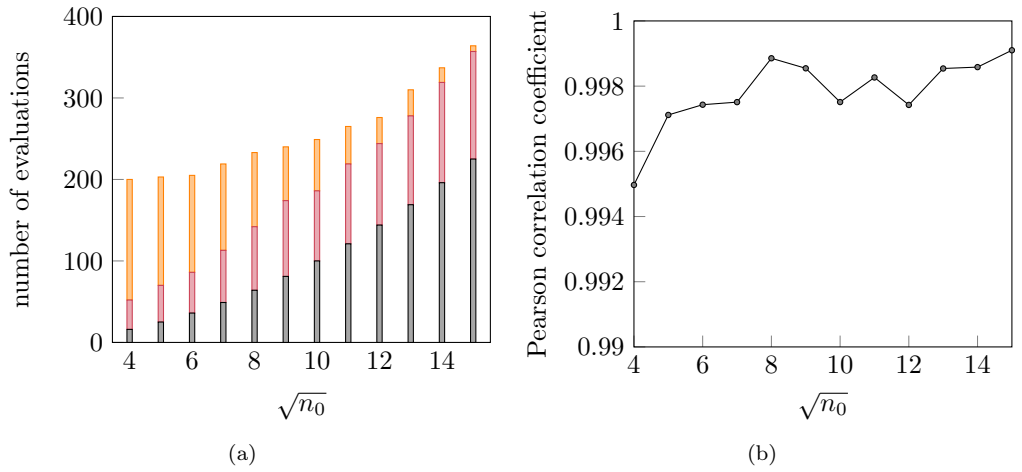

Figure 19. Results of the proposed methodology as a function of the parameter n_0: (a) number of evaluations per step, initial mesh (■), iterative edge detection (■) and localized mesh refinement (■); (b) Pearson correlation coefficients.

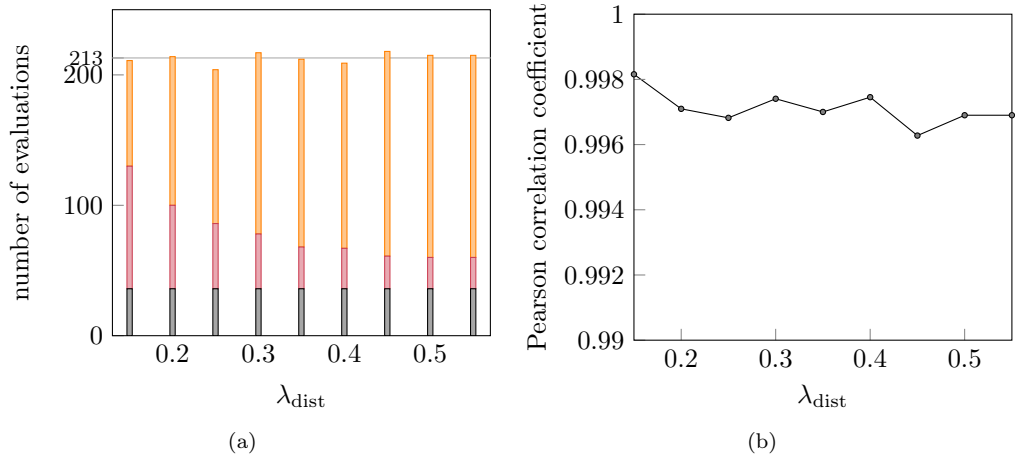

Figure 20. Results of the proposed methodology as a function of the criterion λ_{dist}: (a) number of evaluations per step, initial mesh (■), iterative edge detection (■) and localized mesh refinement (■); (b) correlation coefficient.

6 Industrial application: blade-tip/casing contact

This last section intends to illustrate how the proposed methodology can be applied to industrial problems. The investigated system is a compressor blade undergoing structural contacts. Contrary to other types of applications for which transient phenomena could be of interest—and for which specific numerical developments are required when considering the application of PCE-based techniques [43, 44]—the analysis of rotating machine components is typically focused on steady states, assuming a periodic forcing, which is propitious to the application of the proposed methodology.

6.1 Nonlinear mechanical system

The compressor blade of interest is NASA rotor 37 [45], a transsonic compressor blade which is publicly available [46]. The casing is assumed perfectly rigid and the equation of motion of the blade reads [47]:

$$\mathbf{M}\ddot{\mathbf{x}} + \mathbf{D}\dot{\mathbf{x}} + \mathbf{K}\mathbf{x} + \mathbf{f}_{nl}(\mathbf{x}, \dot{\mathbf{x}}) = \mathbf{f}_{ex}(\omega, t), \tag{30}$$

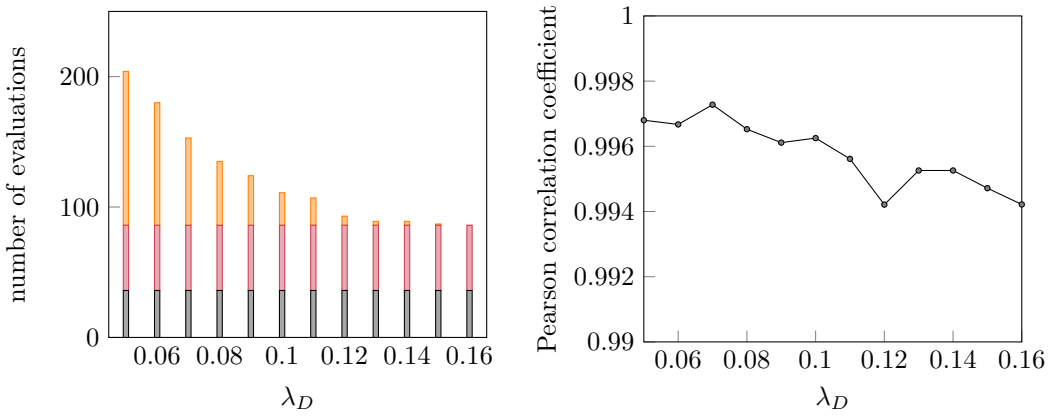

Figure 21. Results of the proposed methodology as a function of the criterion λ_D: (a) number of evaluations per step, initial mesh (■), iterative edge detection (■) and localized mesh refinement (■); (b) correlation coefficient.

where $\mathbf{M}, \mathbf{D}$ and $\mathbf{K}$ are mass, damping and stiffness matrices, respectively. $\mathbf{f}_{ex}(\omega, t)$ is the excitation force of angular frequency ω at a time t, $\mathbf{f}_{nl}(\mathbf{x}, \dot{\mathbf{x}})$ denotes the nonlinear forces and $\mathbf{x}$, $\dot{\mathbf{x}}$ and $\ddot{\mathbf{x}}$ stand for the displacement and its first and second derivatives with respect to time.

The equation of motion is solved with an explicit time integration scheme using a Lagrange multipliers-based algorithm for contact treatment. The Craig-Bampton model reduction technique [48] is employed to reduce the dimension of the system. A modal damping is considered, centrifugal effects are neglected and the blade is clamped at its root. Eight evenly spaced nodes are considered along the blade-tip where contact forces may be applied. To initiate contact with the blade, the casing is progressively ovalized. In order to illustrate the blade response to such contact event, the time response of the blade's leading edge radial displacement with respect to time is depicted in Fig. 22(a). In this figure, transient and steady state parts of the time response are represented by markers ② and ③, respectively. The same quantity is depicted over the last period in Fig. 22(b) where the maximal radial displacement (▬) is highlighted. The steady state maximal radial displacement, denoted $\mathcal{D}(\omega, c)$, is a quantity of interest because the blade's response is mostly associated to its first bending mode. For that reasons, instants for which the radial displacement is maximal correspond to instants where stresses within the blade (in the vicinity of its root) will be maximal.

When looking at the evolution of $\mathcal{D}(\omega, c)$ with respect to key parameters of the system such as the blade angular velocity ω and the blade-tip/casing clearance c, it is evidenced that the response surface of the system is discontinuous, see Fig. 23. The reference response surface pictured in Fig. 23 has been obtained considering a sampling of $2\,\mathrm{rad}\cdot\mathrm{s}^{-1}$ in ω and $10^{-5}\,\mathrm{m}$ in c which represents a total of 6666 evaluations, requiring about 192 hours of computation time (104 s of computation time on average per evaluation).

6.2 gPCE and ME-gPCE approximations

Considering the computational cost of the response surface depicted in Fig. 23, gPCE is first used to approximate it. gPCE coefficients are computed based on a 81 point design of experiments, with a regular grid of 9×9 equidistant points over the domain see (○) in Fig. 24(a). A high value of the gPCE degree is considered: $q = 7$. The corresponding approximated response surface is plotted in Fig. 24(a). The distribution of the error with respect to the reference response surface noted E is plotted in Fig. 24(b). As observed for the Duffing system, gPCE cannot capture the discontinuity of the response surface thus yielding significant errors in the approximation of the response surface.

ME-gPCE is then used to overcome the limitations of gPCE. A decomposition of the random space within 16 rectangular subdomains is performed. Over each of subdomains, gPCE is applied with $q = 2$ using a 9-point uniform DoE. The approximated response surface is shown in Fig. 25(a) using the 6666 reference samples, and the error

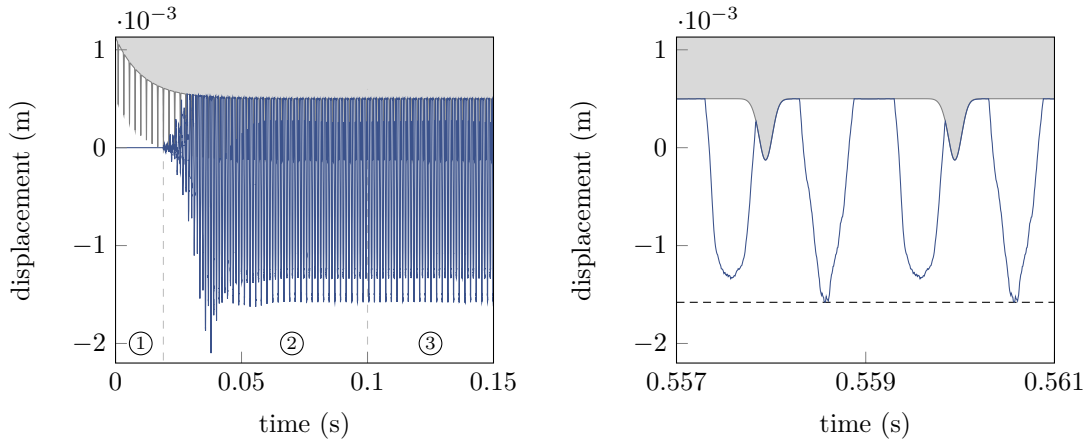

Figure 22. Leading edge radial displacement of the blade: (a) full time response over 125 blade revolutions, contact deformation before contact ① transient response ② and steady state ③; (b) zoom over the last period, maximal radial displacement (▬▪▬).

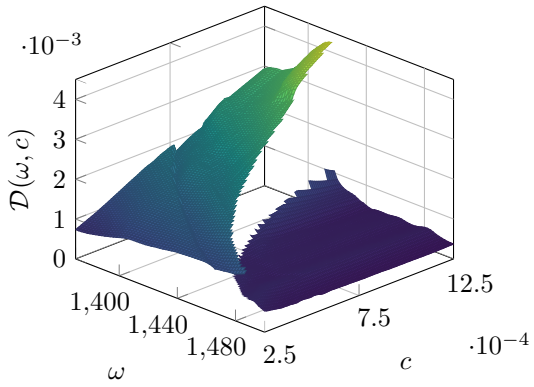

Figure 23. Response surface of the blade-tip/casing system.

distribution is plotted in Fig. 25(b). Same as for Duffing system, ME-gPCE yields: (1) excellent results for each subdomain where the reference response surface is continuous, and (2) significant errors where the reference response surface is discontinuous. ME-gPCE therefore yields more localized errors but still significant errors.

6.3 Application of the proposed methodology

The proposed methodology is used to automatically identify the discontinuity of the response surface before it can be approximated. Using the numerical parameters given in Tab. 2, the number of evaluations of the system's response required to obtain the approximation of the response surface is 94 (split into 36 evaluations on initial mesh, 47 evaluations for the iterative edge detection step and 11 evaluations during the localized mesh refinement step). The detected discontinuity (–●–) is shown in Fig. 26(a). It is in very good agreement with the reference discontinuity (▬). A decomposition of the random space within 2 subdomains is then performed, see Fig. 26(b). From the 94 evaluations, gPCE is applied with DoE composed of 51 and 43 on each subdomain respectively. A degree 4 is considered on each subdomain. The response surface thus obtained is depicted in Fig. 26(c), and the error distribution with respect to the reference response surface is shown in Fig. 26(d).

Overall, the presented results underline that the proposed methodology provides a very accurate representation of the system's response surface. While the associated computational gain is difficult to estimate as it is directly

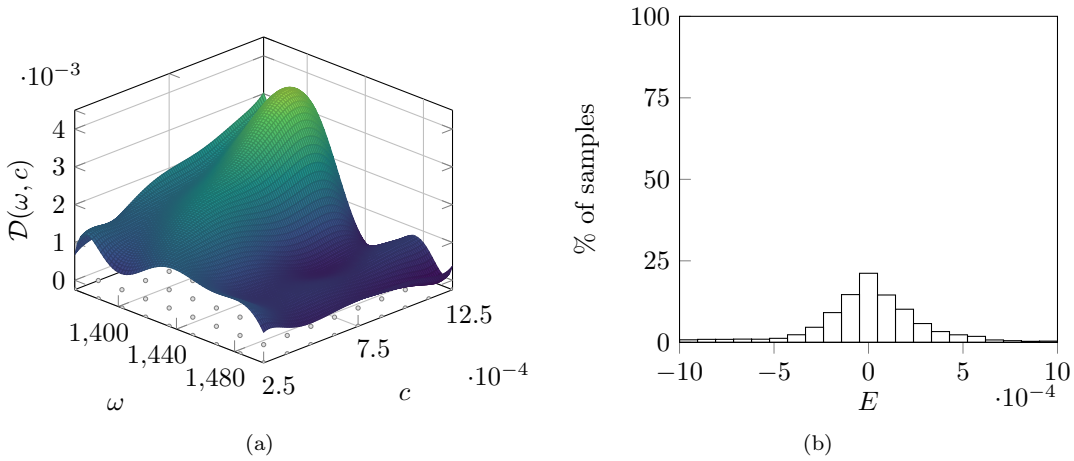

Figure 24. Results of the gPCE for the blade-tip/casing system: (a) response surface approximation from DoE (●); (b) error distributions with respect to the reference response surface (sum of all the columns on the histogram: 97.49 %).

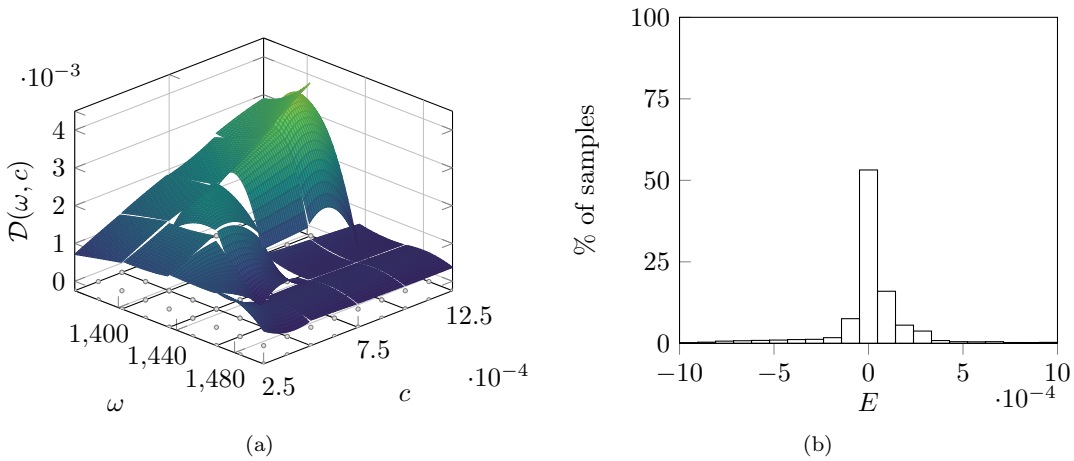

Figure 25. Results of the ME-gPCE for the blade-tip/casing system: (a) response surface approximation from DoE (●); (b) error distributions with respect to the reference response surface (sum of all the columns on the histogram: 97.22 %).

related to the resolution needed by designers for the reference response surface, it is patent that the 94 evaluations needed for the proposed methodology could not lead to an accurate description of the system's response surface.

7 Conclusion

This study focuses on the application of Multi-Element generalized Polynomial Chaos Expansion combined with automatic discontinuity detection to analyze nonlinear systems. The proposed methodology includes an automated detection of discontinuities in order to apply a gPCE approximation on each subdomain. These subdomains are delimited by the detected discontinuities. The decomposition of the random space proposed by the methodology tracks the discontinuities of the discontinuous response surface. gPCE approximations are then performed on each subdomain.

The proposed methodology is applied to a circular discontinuity and to the academic Duffing system including one or two discontinuities. These applications yield accurate results on both phases of the methodology: discontinuities detection and response surface approximation. It highlights that the accurately detected discontinuities then allows

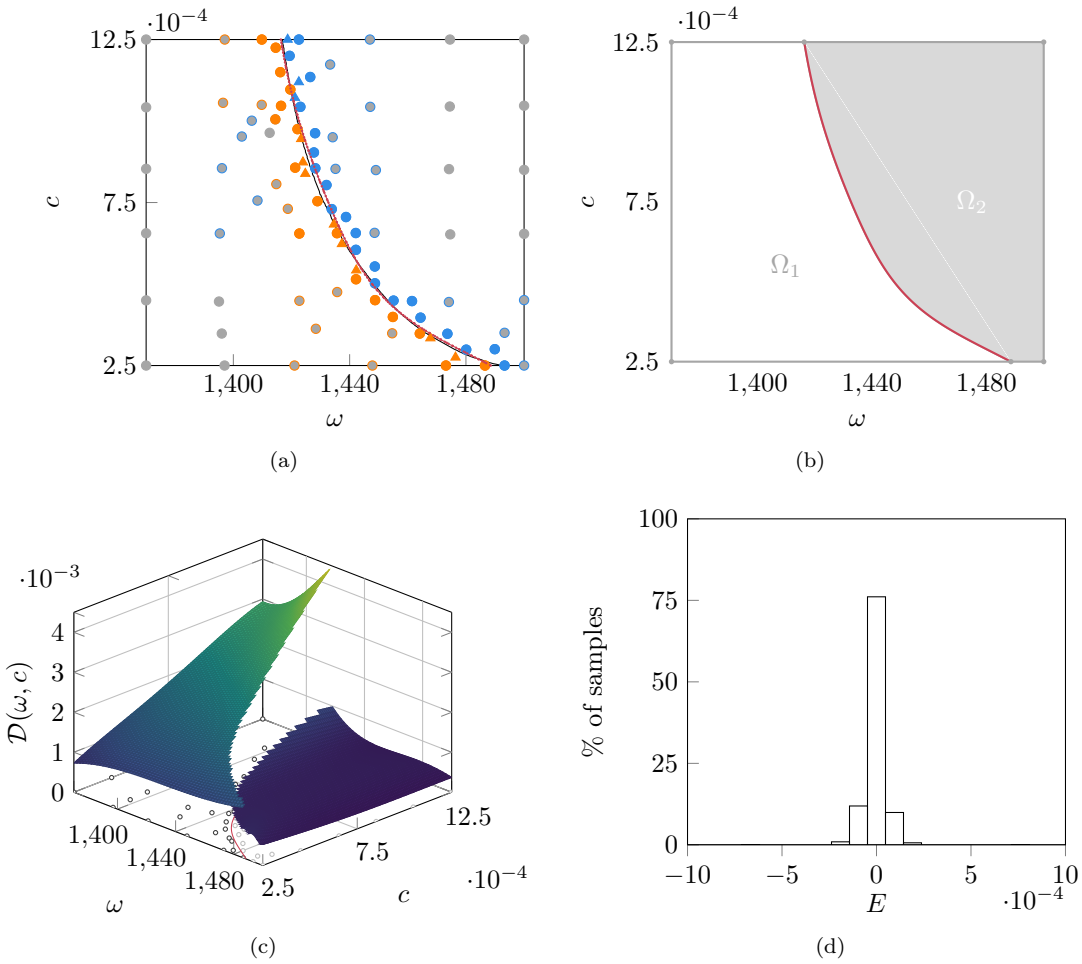

Figure 26. Results of the proposed methodology for the blade-tip/casing system: (a) automated discontinuity detection; (b) domain decomposition; (c) response surface approximation; (d) error distributions with respect to the reference response surface (sum of all the columns on the histogram: 99.55 %). Initial mesh (●), points of $\mathcal{G}_{p+}^{(k_{\text{ed}})}$ (●) and $\mathcal{G}_{p-}^{(k_{\text{ed}})}$ (●), points added during the localized mesh refinement step (▲) with label $+1$ (○) or -1 (○). Detected (-●-) and reference (—) discontinuities.

a good agreement of the response approximation compared to reference response surface. Moreover, the proposed methodology requires no additional evaluations for the ME-gPC approximation, only the evaluations performed in the first phase are used. An analysis of the influence of the methodology's parameters is carried out, it shows the robustness of the methodology and the effect of the parameters on the computational cost and the quality of the discontinuities and approximations. Finally, while the proposed methodology is currently limited to two-dimensional problems, its successfull application to an industrial system relating to turbomachinery underlines its applicability to complex engineering systems.

Acknowledgment

This research was undertaken thanks to funding from the Canada Research Chairs Program.

References

[1] B. Sudret. "Global sensitivity analysis using polynomial chaos expansions". In: Reliab. Eng. Syst. Saf. Vol. 93, No. 7 (2008). doi: 10.1016/j.ress.2007.04.002, 964–979.

[2] A. Saltelli, M. Ratto, T. Andres, F. Campolongo, J. Cariboni, D. Gatelli, M. Saisana, and S. Tarantola. Global sensitivity analysis: the primer. doi: 10.1002/9780470725184. 2008.

[3] R. G. Ghanem and P. D. Spanos. Stochastic finite elements: a spectral approach. doi: 10.1007/978-1-4612-3094-6. 1991.

[4] R. Ghanem. "Ingredients for a general purpose stochastic finite elements implementation". In: Comput. Methods Appl. Mech. Eng. Vol. 168, No. 1 (1999). doi: 10.1016/S0045-7825(98)00106-6, 19–34.

[5] N. Wiener. "The Homogeneous Chaos". In: American Journal of Mathematics Vol. 60, No. 4 (1938). doi: 10.2307/2371268, 897–936.

[6] O. P. Le Maître, M. T. Reagan, H. N. Najm, R. G. Ghanem, and O. M. Knio. "A Stochastic Projection Method for Fluid Flow: II. Random Process". In: J. Comput. Phys. Vol. 181, No. 1 (2002). doi: 10.1006/jcph.2002.7104, 9–44.

[7] J. Philippe, F. Thouverez, L. Blanc, and M. Gruin. "Vibratory behavior prediction of mistuned stator vane clusters: An industrial application". In: Comput. Struct. Vol. 196 (2018). doi: 10.1016/j.compstruc.2017.11.003, 12–23.

[8] K. Szepietowska, B. Magnain, I. Lubowiecka, and E. Florentin. "Sensitivity analysis based on non-intrusive regression-based polynomial chaos expansion for surgical mesh modelling". In: Struct. Multidiscip. Optim. Vol. 57, No. 3 (2018). doi: 10.1007/s00158-017-1799-9, 1391–1409.

[9] J. Dréau, B. Magnain, F. Nyssen, and A. Batailly. "Polynomial chaos expansion for permutation and cyclic permutation invariant systems: Application to mistuned bladed disks". In: J. Sound Vib. Vol. 503 (2021). doi: 10.1016/j.jsv.2021.116103, 116103.

[10] D. Xiu and G. E. Karniadakis. "The Wiener-Askey polynomial chaos for stochastic differential equations". In: SIAM J. Sci. Comput. Vol. 24, No. 2 (2002). doi: 10.1137/S1064827501387826, 619–644.

[11] B. Sudret and A. Der Kiureghian. *Stochastic Finite Element Methods and Reliability A State-of-the-Art Report.* Tech. rep. UCB/SEMM-2000/08. Department of Civil and Environmental Engineering, University of California, Berkeley, 2000.

[12] M. Berveiller, B. Sudret, and M. Lemaire. "Stochastic finite element: a non intrusive approach by regression". In: Eur. J. Comp. Mech. Vol. 15, No. 1-3 (2006). doi: 10.3166/remn.15.81-92, 81–92.

[13] X. Wan and G. E. Karniadakis. "An adaptive multi-element generalized polynomial chaos method for stochastic differential equations". In: J. Comput. Phys. Vol. 209, No. 2 (2005). doi: 10.1016/j.jcp.2005.03.023, 617–642.

[14] E. Sarrouy, O. Dessombz, and J.-J. Sinou. "Piecewise polynomial chaos expansion with an application to brake squeal of a linear brake system". In: J. Sound Vib. Vol. 332, No. 3 (2013). doi: 10.1016/j.jsv.2012.09.009, 577–594.

[15] X. Wan and G. E. Karniadakis. "Multi-Element Generalized Polynomial Chaos for Arbitrary Probability Measures". In: SIAM J. Sci. Comput. Vol. 28, No. 3 (2006). doi: 10.1137/050627630, 901–928.

[16] X. Wan and G. E. Karniadakis. "Long-term behavior of polynomial chaos in stochastic flow simulations". In: Comput. Methods Appl. Mech. Eng. Vol. 195, No. 41 (2006). doi: 10.1016/j.cma.2005.10.016, 5582–5596.

[17] L. Nechak, S. Berger, and E. Aubry. "Prediction of Random Self Friction-Induced Vibrations in Uncertain Dry Friction Systems Using a Multi-Element Generalized Polynomial Chaos Approach". In: J. Vib. Acoust. Vol. 134, No. 4 (2012). doi: 10.1115/1.4006413.

[18] R. Archibald, A. Gelb, and J. Yoon. "Polynomial Fitting for Edge Detection in Irregularly Sampled Signals and Images". In: SIAM J. Numer. Anal. Vol. 43, No. 1 (2005). doi: 10.1137/S0036142903435259, 259–279.

[19] A. Gorodetsky and Y. Marzouk. "Efficient Localization of Discontinuities in Complex Computational Simulations". In: SIAM J. Sci. Comput. Vol. 36, No. 6 (2014). doi: 10.1137/140953137, A2584–A2610.

[20] K. Sargsyan, C. Safta, B. Debusschere, and H. Najm. "Uncertainty Quantification given Discontinuous Model Response and a Limited Number of Model Runs". In: SIAM J. Sci. Comput. Vol. 34, No. 1 (2012). doi: 10.1137/100817899, B44–B64.

[21] C. Snoun, B. Bergeot, and S. Berger. "Prediction of the dynamic behavior of an uncertain friction system coupled to nonlinear energy sinks using a multi-element generalized polynomial chaos approach". In: Eur. J. Mech. A. Solids Vol. 80 (2020). doi: 10.1016/j.euromechsol.2019.103917, 103917.

[22] J. D. Jakeman, A. Narayan, and D. Xiu. "Minimal multi-element stochastic collocation for uncertainty quantification of discontinuous functions". In: J. Comput. Phys. Vol. 242 (2013). doi: 10.1016/j.jcp.2013.02.035, 790–808.

[23] Y. V. Halder, B. Sanderse, and B. Koren. "An Adaptive Minimum Spanning Tree Multielement Method for Uncertainty Quantification of Smooth and Discontinuous Responses". In: SIAM J. Sci. Comput. Vol. 41, No. 6 (2019). doi: 10.1137/18M1219643, A3624–A3648.

[24] P. Pettersson, A. Doostan, and J. Nordström. "Level set methods for stochastic discontinuity detection in nonlinear problems". In: J. Comput. Phys. Vol. 392 (2019). doi: 10.1016/j.jcp.2019.04.053, 511–531.

[25] J. Foo, X. Wan, and G. E. Karniadakis. "The multi-element probabilistic collocation method (ME-PCM): Error analysis and applications". In: J. Comput. Phys. Vol. 227, No. 22 (2008). doi: 10.1016/j.jcp.2008.07.009, 9572–9595.

[26] A. Narayan and D. Xiu. "Stochastic Collocation Methods on Unstructured Grids in High Dimensions via Interpolation". In: SIAM J. Sci. Comput. Vol. 34, No. 3 (2012). doi: 10.1137/110854059, A1729–A1752.

[27] A. C. Hindmarsh. "ODEPACK, A systemized collection of ODE solvers". In: Scientific computing (1983), 55–64.

[28] L. Petzold. "Automatic Selection of Methods for Solving Stiff and Nonstiff Systems of Ordinary Differential Equations". In: SIAM Journal on Scientific and Statistical Computing Vol. 4, No. 1 (1983). doi: 10.1137/0904010, 136–148.

[29] O. Le Maître, H. Najm, R. Ghanem, and O. Knio. "Multi-resolution analysis of Wiener-type uncertainty propagation schemes". In: J. Comput. Phys. Vol. 197, No. 2 (2004). doi: 10.1016/j.jcp.2003.12.020, 502–531.

[30] L. Piegl and W. Tiller. The NURBS Book. doi: 10.1007/978-3-642-59223-2. 1997.

[31] C. M. Bishop and N. M. Nasrabadi. Pattern recognition and machine learning. Vol. 4. 4. 2006.

[32] C. Cortes and V. Vapnik. "Support-vector networks". In: Mach. Learn. Vol. 20 (1995). doi: 10.1007/BF00994018, 273–297.

[33] C.-C. Chang and C.-J. Lin. "LIBSVM: A Library for Support Vector Machines". In: ACM Trans. Intell. Syst. Technol. Vol. 2, No. 3 (2011). doi: 10.1145/1961189.1961199.

[34] O. P. Le Maître and O. M. Knio. Spectral methods for uncertainty quantification: with applications to computational fluid dynamics. doi: 10.1007/978-90-481-3520-2. 2010.

[35] W. J. Gordon and C. A. Hall. "Construction of curvilinear co-ordinate systems and applications to mesh generation". In: Int. J. Numer. Methods Eng. Vol. 7, No. 4 (1973). doi: 10.1002/nme.1620070405, 461–477.

[36] W. J. Gordon and C. A. Hall. "Transfinite element methods: blending-function interpolation over arbitrary curved element domains". In: Numer. Math. Vol. 21 (1973). doi: 10.1007/BF01436298, 109–129.

[37] J. F. Thompson, B. K. Soni, and N. P. Weatherill. Handbook of grid generation. doi: 10.1201/9781420050349. 1998.

[38] M. Held and R. M. Karp. "The Traveling-Salesman Problem and Minimum Spanning Trees". In: Operations Research Vol. 18, No. 6 (1970). doi: 10.1287/opre.18.6.1138, 1138–1162.

[39] J. B. Kruskal. "On the Shortest Spanning Subtree of a Graph and the Traveling Salesman Problem". In: Proceedings of the American Mathematical Society Vol. 7, No. 1 (1956). doi: 10.2307/2033241, 48–50.

[40] M. Bellmore and G. Nemhauser. "The Traveling Salesman Problem: A Survey". In: Oper. Res. Vol. 16, No. 3 (1968). doi: 10.1287/opre.16.3.538, 538–558.

[41] S. Khattri. "Grid Generation and Adaptation by Functionals". In: Computational and Applied Mathematics Vol. 26 (2006).

[42] W. Huang, L. Kamenski, and R. D. Russell. "A Comparative Numerical Study of Meshing Functionals for Variational Mesh Adaptation". In: Journal of Mathematical Study Vol. 48, No. 2 (2015). doi: 10.4208/jms.v48n2.15.04, 168–186.

[43] B. Bhattacharyya, E. Jacquelin, and D. Brizard. "Uncertainty Quantification of Stochastic Impact Dynamic Oscillator Using a Proper Orthogonal Decomposition-Polynomial Chaos Expansion Technique". In: J. Vib. Acoust. Vol. 142, No. 6 (2020). doi: 10.1115/1.4047359.

[44] B. Bhattacharyya, E. Jacquelin, and D. Brizard. "Stochastic analysis of a crash box under impact loading by an adaptive POD-PCE model". In: Struct. Multidiscip. Optim. Vol. 65, No. 8 (2022). doi: 10.1007/s00158-022-03299-6, 229.

[45] L. Reid and R. D. Moore. *Design and overall performance of four highly loaded, high speed inlet stages for an advanced high-pressure-ratio core compressor*. Tech. rep. NASA-TP-1337. NASA Lewis Research Center Cleveland, OH, United States, 1978.

[46] S. Kojtych and A. Batailly. *A catalogue of open NASA blade models*. Version 1.0. HAL id: hal-03945336. 2023.

[47] M. Legrand, A. Batailly, B. Magnain, P. Cartraud, and C. Pierre. "Full three-dimensional investigation of structural contact interactions in turbomachines". In: J. Sound Vib. Vol. 331, No. 11 (2012). doi: 10.1016/j.jsv.2012.01.017, 2578–2601.

[48] R. R. Craig and M. C. C. Bampton. "Coupling of Substructures for Dynamic Analyses". In: AIAA Journal Vol. 6, No. 7 (1968). doi: 10.2514/3.4741, 1313–1319.